CLAP AND FLING INTERACTION OF BRISTLED WINGS: EFFECTS OF VARYING REYNOLDS NUMBER AND BRISTLE SPACING ON FORCE GENERATION AND FLOW STRUCTURES

By

VISHWA TEJA KASOJU

Bachelor of Engineering in Mechanical Engineering

Osmania University

Hyderabad, India

2013

Submitted to the Faculty of the
Graduate College of the
Oklahoma State University
in partial fulfillment of
the requirements for
the Degree of
MASTER OF SCIENCE
May, 2017

CLAP AND FLING INTERACTION OF BRISTLED WINGS: EFFECTS OF VARYING REYNOLDS NUMBER AND BRISTLE SPACING ON FORCE GENERATION AND FLOW STRUCTURES

Thesis Approved:

Dr. Arvind Santhanakrishnan

Thesis Adviser

Dr. Khaled Sallam

Dr. Brian Elbing

ACKNOWLEDGEMENTS

Firstly, I would like to express my sincere gratitude to my advisor, mentor Dr. Arvind Santhanakrishnan for the continuous support in my study and related research, for his patience, motivation, and immense knowledge. I am particularly grateful to him for enlightening me the first glance of research. His guidance helped me all the time in research and writing of this thesis. I could not have imagined having a better advisor and mentor for my Master's study. I am very happy to continue my Ph.D. study under his guidance.

I would like to thank my thesis committee: Dr. Khaled Sallam and Dr. Brian Elbing for their insightful comments and encouragement.

I thank my fellow labmates Chris Terrill, Manikantam Gaddam, Hong Kuan Lai and Milad Samaee for being there for me whenever needed. I particularly thank Chris Terrill for helping me with starting my research. I extend my thanks to Mitchell ford, Skyler Jacob and Colton Sullivan for their support.

Last but not the least, I would like to thank my family: my parents and sister for supporting me throughout this journey.

This research was supported by the National Science Foundation (CBET 1512071) awarded to Dr. Arvind Santhanakrishnan.

Name: VISHWA TEJA KASOJU

Date of Degree: MAY 2017

Title of Study: CLAP AND FLING INTERACTION OF BRISTLED WINGS: EFFECTS OF VARYING REYNOLDS NUMBER AND BRISTLE SPACING ON FORCE GENERATION AND FLOW STRUCTURES

Major Field: MECHANICAL ENGINEERING

Abstract: The smallest flying insects with body lengths under 1 mm, such as thrips and fairyflies, typically show the presence of long bristles on their wings. Thrips have been observed to use wing-wing interaction via 'clap and fling' for flapping flight at low Reynolds number (*Re*) on the order of 10, where a wing pair comes into close contact at the end of upstroke and fling apart at the beginning of downstroke. We examined the effects of varying the following parameters on force generation and flow structures formed during clap and fling: (1) *Re* ranging from 5 to 15 for a bristled wing pair (G/D=17) and a geometrically equivalent solid wing pair; and (2) ratio of spacing between bristles to bristle diameter (G/D) for *Re*=10. The G/D ratio in 70 thrips species were quantified from published forewing images. Scaled-up physical models of three bristled wing pairs of varying G/D (5, 11, 17) and a solid wing pair (G/D=0) were fabricated. A robotic model was used for this study, in which a wing pair was immersed in an aquarium tank filled with glycerin and driven by stepper motors to execute clap and fling kinematics. Dimensionless lift and drag coefficients were determined from strain gauge measurements. Phase-locked particle image velocimetry (PIV) measurements were used to examine flow through the bristles. Chordwise PIV was used to visualize the leading edge vortex (LEV) and trailing edge vortex (TEV) formed over the wings during clap and fling. With increasing G/D, larger reduction was observed in peak drag coefficients as compared to reduction in peak lift coefficients. Net circulation, defined as the difference in circulation (strength) of LEV and TEV, diminished with increasing G/D. Reduction in net circulation resulted in reducing lift generated by bristled wings as compared to solid wings. Leaky, recirculating flow through the bristles provided large drag reduction during fling of a bristled wing pair. If flight efficiency is defined as the ratio of lift to drag, largest peak lift to peak drag ratios were obtained in bristled wings as compared to the solid wings across the entire range of *Re* and G/D tested.

TABLE OF CONTENTS

Chapter Page

LIST OF TABLES

Table Page

LIST OF FIGURES

CHAPTER I

INTRODUCTION

1.1. Motivation

Nature comprises of large variety of insects ranging from fairy flies (body length as small as 250 microns)[1] to hawkmoth (body length~250 mm). Most of these insects flap their wings rapidly at about 200 Hz or more and generate necessary lift force required to fly. However, in the past little was known about how these animals were capable in generating enough lift force to counter their body weight [2]–[5]. Thus, it became necessary to understand the force generation during insect flight. During 1930‘s there was question in the research community about how a bumble bee flies. Conventional aerodynamic theory (limited to steady flows) showed that it is impossible for a bumblebee to fly, yet it is well known that bumblebee is capable of flight. This finding led to an open-question that was known as the “bumblebee paradox”, and it remained unaddressed until the late 1990’s. Professor Charles Ellington’s discovery in 1984 [4] that aerodynamic lift generation in flapping flight was primarily achieved via the formation of a stable leading edge vortex (thereafter referred to as dynamic stall) showed the importance of considering unsteady effects for the first time. A large number of studies since then have expanded on our knowledge of aerodynamics of flapping flight in insects ([2], [5], [6]). However, most of the research have been focused on larger scale insects of body lengths > 1 mm ([2], [3], [6], [7]). Comparatively fewer studies have examined flight in tiny insects of body lengths less than 1mm and found that

aerodynamic forces generated in smaller scale insects differ largely from those of larger scale insects. Tiny insects such as fairy flies and thrips have wingspans lesser than 0.5 mm. At these small scales, viscous forces are dominant in comparison to inertial forces (low Reynolds number *Re* on the order of 10). Thus, we can expect a considerable increase in energetic demand needed to flap their wings in the face of increased resistive forces (drag) experienced by the wings. However, field observations in tiny insects such as thrips [8] provide evidence of their capabilities of directed flight as well as large-scale dispersal and migration. Studies of the aerodynamics of flapping flight in tiny insects can provide us with a fundamental understanding of the physical mechanisms that are responsible for sustaining force generation at these smaller scales.

1.2. Specific aims

Tiny insects of length scales less than 1 mm, such as thrips, fairyflies and parasitoid wasps, are reported to fly at Reynolds number (*Re*; defined as ratio of inertial to viscous forces) on the order of 10 [8] and use wing-wing interaction via the 'clap and fling' mechanism as a part of their flight kinematics. Several researchers [3], [4] have looked into the aerodynamics of solid/flat-plate wing models mimicking clap-fling kinematics and observed the formation of a leading edge vortex at the start of fling, which was attributed to generate lift force required to fly. However, wings of tiny insects show the presence of fringes/bristles or hair-like setae attached to a solid membrane. Some studies ([8]–[10]) have investigated the effect of bristles on aerodynamics of flapping flight at low *Re* and reported predominant decrease in drag force for bristled wings as compared to solid wings. However, the effect of bristles on lift generation has not been previously examined.

The central hypothesis of this study is that for a wing pair performing 'clap and fling' kinematics at low *Re* on the orders of 1-10, both lift and drag forces will decrease for bristled wings as compared to solid wings. Further, we hypothesize that drag reduction with

bristled wings will be larger in proportion to their effect on lift reduction, such that lift over drag ratio will be larger for bristled wings as compared to solid wings of equivalent geometry. These hypotheses will be tested using the following specific aims (SAs).

SA 1: Use a dynamically scaled robotic clap and fling simulator to quantify the aerodynamic forces and flow structures for solid and bristled wing physical models under varying *Re* from 5-15.

Aerodynamic forces will be measured using strain gauges on physical models of solid and bristled wing pairs incorporated into an existing robotic clap and fling model. The ratio of gap between a pair of bristles (G) to the bristle diameter will be maintained constant (G/D=17). 2D time-resolved particle image velocimetry (TR-PIV) will be used to characterize flow structures along the central chordwise plane, while 2D phase-locked PIV (PL-PIV) will be used to characterize the flow through the bristles along the spanwise direction. TR-PIV data will be used to determine strength (circulation) of the leading edge vortex (LEV) and trailing edge vortex (TEV). PL-PIV data will be used to determine leakiness of flow through the bristled wing model, defined as the ratio of reverse/leaking viscous flow rate through the bristles to the inviscid/ideal flow rate. The results of these analyses will be used to examine how force generation is impacted by: (a) circulation of the LEV and TEV, and (b) leakiness of bristled wing.

SA 2: (a) Conduct morphometric analysis of published data of bristled wings in the order Thysanoptera and quantify the biological variability in G/D ratio. (b) Design bristled wing models with biologically relevant G/D and quantify the aerodynamic forces and flow structures generated by these wing models at *Re*=10.

Morphological analysis of published images of bristled wings in the order Thysanoptera will be conducted using ImageJ software (National Institutes of Health, Bethesda, MD) to quantify the biological variation of the gap to diameter ratio (G/D). Two physical wing models will be

designed with varying G/D ratio within the observed biological range and tested using the clap and fling robotic model. Aerodynamic forces will be measured using strain gauges on these wing models at *Re*=10. TR-PIV and PL-PIV will be performed along chordwise and spanwise directions, respectively. Analyses of TR-PIV, PL-PIV and force data will be conducted similar to SA1 to examine the implications of varying G/D on aerodynamic forces, lift to drag ratio, leakiness, and LEV/TEV circulation.

The outcomes of the proposed study are expected to show for the first time that bristled wings decrease the drag force disproportionally in comparison to lift reduction for clap and fling wing-wing interaction at low *Re* in the range of 5-15. In addition, the results from this study will identify the aerodynamic implications of varying the spacing between bristles on force generation and flow structures.

1.3. Significance

1.3.1. Engineering

Places of potential targets (places that are densely populated such as shopping malls, play grounds etc.,) need to be secured and placed under high security surveillance. While drones are used to complete these tasks, there are possibilities of attracting attention due to their larger size. In this context, micro aerial vehicles (MAVs) can serve the purpose while minimizing the possibility of human detection. MAVs are small-scale unmanned aerial vehicles (miniature 'drones') with overall dimensions not larger than 15 cm and flight speed of 10m/s [11]. Designing such a small, unmanned, slow flying aerial vehicle is of high importance in the field of military and civilian applications. MAVs equipped with video cameras and sensors could be used for gathering intelligence in hazardous and remote areas performing surveillance and reconnaissance [12]. In order to accomplish these tasks, MAVs are needed to be easily maneuverable with efficient propulsion to fly onboard with payloads. While conventional methods of lift generation

(use of propellers) has proved to be inefficient in terms of required capability at these smaller scales [12], alternative ways for efficient propulsion of MAVs are of high importance for ongoing research. Since these MAVs fly at low *Re* due to their small size, biomimetic design of MAV propulsion mimicking aerodynamic mechanisms used by tiny insects could provide an alternative, efficient means of propulsion as compared to existing propeller choices.

1.3.2. Agricultural and ecological

Tiny insects such as thrips perform important ecological roles such as: (i) active pollinators during their feeding process [13]; (ii) biological vectors for transmitting plant viruses such as *Tospovirus, Ilarvirus, Carmovirus* into plants [14][15]; and (iii) invasive pests of commercially important plants such as tomato, onion, peanut [8], to the extent of damaging the plants by direct feeding. Indications of such effects are leaf silvering [15]. In addition, they are also observed to exhibit complex social behavior such as forming allies and group defense [16]. Hence, studying the physics underlying their flapping flight can assist in understanding their dispersal strategies and improve techniques used in their eradication or mitigation.

CHAPTER II

LITERATURE REVIEW

2.1. Flapping Flight

The question about how do insects fly practically goes decades back. There have been many studies on aerodynamics of flapping insect in both experimental and computational worlds. These studies have given a basic idea on flapping flight in insects. However, the question still need precise explanations. Some of the studies will be discussed in coming sections [8], [17], [18]. Several researchers in there works have used various flow visualizations techniques to address the correlation between force generation, flow structures and pressure distribution on the insect wings [2], [8], [18], [19]. Each of there works has brought us a step closer to finding ways to answer the question. In addition, they also pose more challenges for future works.

2.1.1. Steady vs unsteady models

Reviewing the literature on insects have shown that our nature contains large variety of insects ranging from fruit fly, *Drosophila melanogaster* [5], [20] to hawk moth, *Manduca sexta* ([2], [19], [21], [22]). However, limited information is available on these insects about how they hop, fly or walk. Early twentieth century was said to be time where scientist started focusing on exploring the physics behind insect flight. The first question asked was can the conventional

quasi-steady aerodynamic theory be applied to predict the forces generated by flapping wing? Literature shows that initial attempts in assuming quasi-steady theory on flapping flight was a failure and this posed a major challenge to researchers [5], [23]. In addition, there was a feeling among the research community that insects use some unsteady mechanism to generate lift. In order to verify these claims, Weis- Fogh [24] presented a logical exercise, which was discussed very well in his paper. The results concluded that steady state models were adequate to study the physics behind flapping mechanism for most insects. However, for few insects such as *E. formosa*, the use of steady-state model has failed. This led them to look on to the unsteady fluid mechanics involved in the flapping flight that enables generation of high lift forces. Later Ellington [25] noticed the flapping flights of various insects and assumed that the unsteady aerodynamics mechanism is characterized based on the kinematics of the wing, wing morphology and flow structures being generated.

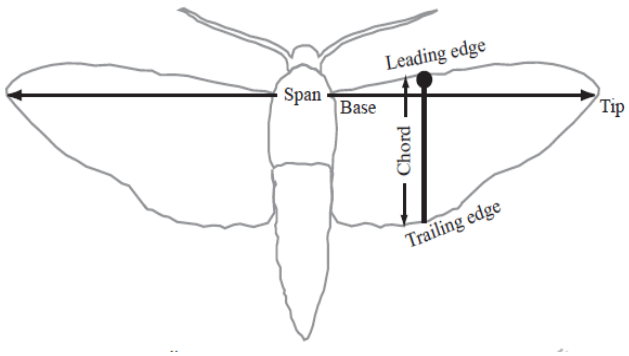

Figure 1: Terminology: Sketch of an stretched out insect showing wing tip, wing span, leading edge and trailing edge [19].

2.2. Terminology

In order to distinguish between fixed wing and flapping flight, a terminology was developed for flapping flight based on the fixed wing aerodynamics. *Figure* 1 shows the sketch of an insect [19]. From the *Figure 1*, 'wing length' represents the length from base to tip the wing. 'Wing

span' represents the length between the tip of the wings when the wings are stretched out laterally. In addition, wing span is also represented as twice the wing length by ignoring the width of the animal. 'Wing chord' represents the vertical distance between leading and trailing edge at any position along the span of the wing. 'Aspect ratio' is defined as the non-dimensional ratio of wing span to wing chord. 'Angle of attack' is defined as the angle that wing chord makes with respect to the free stream velocity direction.

The flight of these insects can be categorized based on a non-dimensional quantity, Reynolds number (*Re*). Reynolds number (*Re*) is the measure of viscous forces to inertial forces and given by the equation $Re = \rho LU/\mu$ where ρ is the density of air, μ is the dynamic viscosity of air, L is the chord length of the wing and U is the wing tip velocity. Reynolds number (*Re*) of the insect ranges in the order 10^1-10^4.

2.3. Characteristics featuring unsteady mechanisms

As discussed in the section 2.1.1, unsteady aerodynamics mechanism were characterized based on the kinematics of the wing, wing morphology and flow structures being generated.

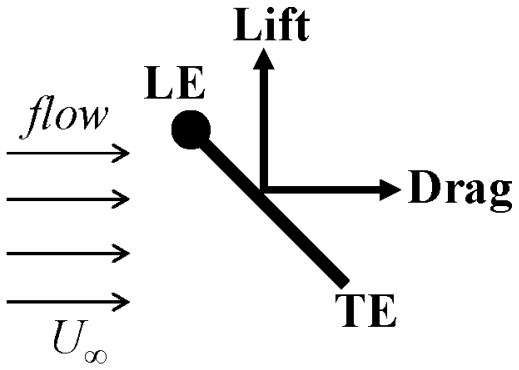

Figure 2: Sectional view of an insect wing shown at an angle. The pointed head of the matchstick indicates the leading edge (LE) and the tail indicates the trailing edge (TE). Lift force is represented in vertical direction and drag force in the horizontal direction.

2.3.1. Flow structures and aerodynamic force generation

Figure 2 shown above represents the sectional view of an insect wing. The matchstick represents the chord line with the pointed head representing the leading edge (LE) and the tail represents the trailing edge (TE). The surrounding fluid is moving in horizontal direction with a velocity U_∞, thereby imparting horizontal, vertical force which represents as drag, lift force respectively.

When a wing translates in an inviscid fluid at particular angle of attack, it is assumed that the fluid gets slightly deflected but would move in the same direction as the surrounding flow. Hence the stagnation point is somewhere on the top surface of the wing section. While under viscous conditions, the flow was observed to be attached in the direction of trailing edge, thereby creating stagnation point at the trailing edge. In addition, there was net force generated in the direction perpendicular to fluid flow. Considering this, Martin Wilhelm Kutta developed a theory, which states that there was a bound circulation on the wing, which was causing the fluid to flow tangentially from the trailing edge. Thereby generating the lift force. This theory was named as 'Kutta condition' [19]. When Kutta condition for a wing is satisfied, the vorticity generated at the trailing edge is zero.

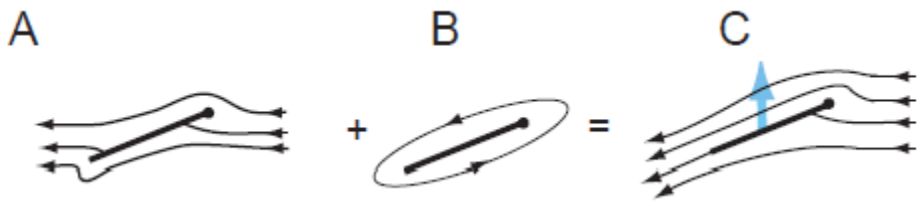

Figure 3: Kutta condition. Sum of A) Ideal flow around an airfoil placed in inviscid fluid, B) Assumed, circulation around the airfoil under viscous condition C) Creates a smooth, tangential flow at trailing edge [19].

In addition, as the wing increases the angle of attack, the fluid flow was observed to separate from the leading edge but it reattaches before reaching the trailing edge, thus satisfying the kutta

condition and also creating a huge vortex. This vortex was called Leading edge vortex. There was an intuition that increasing the angle of attack of a wing could impart greater downward momentum to the fluid, thereby enhancing the lift force. Several computational and experimental studies have identified leading edge vortex to be important for insect wings in generating the forces thereby supporting the intuition.

2.3.2. Wing Kinematics

The aerodynamics associated with flapping insect flight features unsteady motions throughout its wing stroke such as clap and fling mechanism, Wagner effect, delayed stall. Each of them are described briefly below.

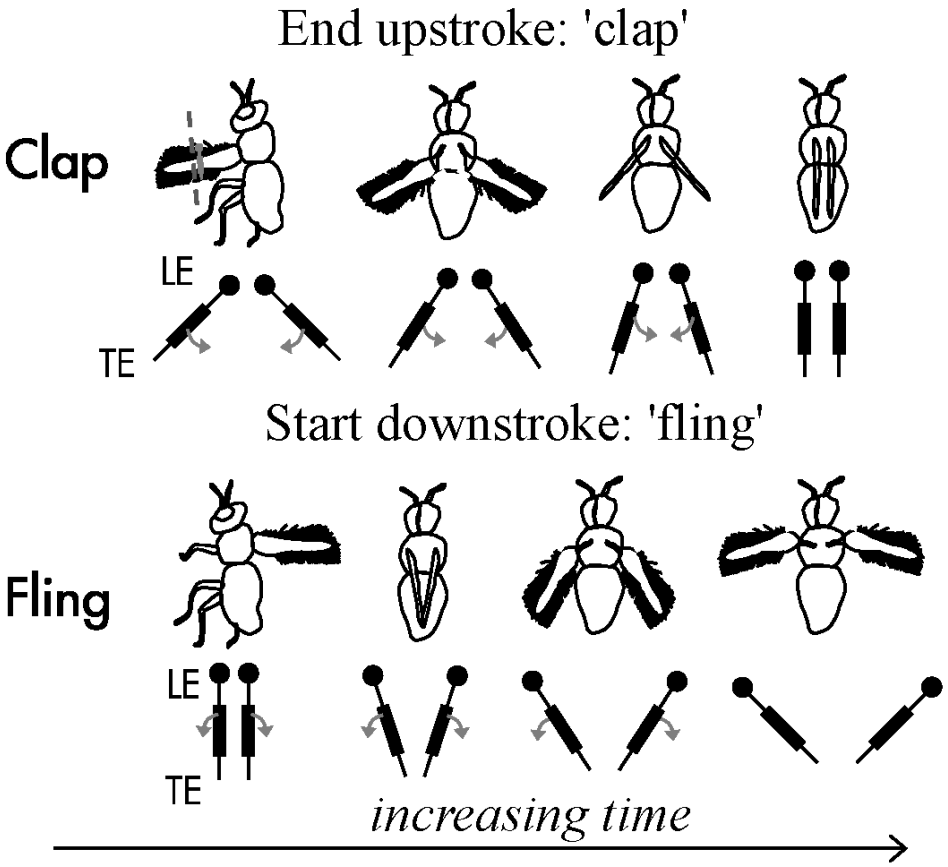

Figure 4: Clap and fling mechanism: A) Clap: At the beginning of the upstroke, the wings rotate together with respect to leading edges and bring the wings close to each other. B) Fling: At the beginning of down stroke, the wings rotate with respect to trailing edges and peel them apart.

2.3.2.1. Clap and fling mechanism

After observing flapping flight of insects such as *E. Formosa*, Weis-Fogh [24] proposed an idea that insects employ a common flapping mechanism called as ‘clap and fling’ during their flapping cycle. Later many other researchers [26] reported to observe clap and fling in other tiny insects like greenhouse whitefly *Tri- aleurodes vaporariorum* [27] , *Thrips physapus* [28], parasitoid wasps *Muscidifurax raptor* and the jewel wasp *Nasonia vitripennis* [29]. Clap and fling mechanism is sometimes referred as ‘Weis-Fogh mechanism’.

During end of upstroke of a flapping flight, insects are noticed to rotate their wings with respect to leading edge and come close together. This is termed as ‘clap’. Some insects were observed to touch their wings each other at the end of clap. While at the start of upstroke, insects were observed to rotate their wings with respect to trailing edge and fling the wings apart. Hence, this is termed as ‘fling’. This mechanism was proposed as one of the reason for augmentation in lift force generation during flapping flight.

2.3.2.2. Wagner effect

Aerodynamic forces acting on a wing that started impulsively from rest at an inclination are lower than the values predicted by quasi-steady models. There was a delay before the forces reach the steady-state value. This was first proposed by Wagner (1925) and later studied experimentally by Walker (1931).

As discussed in the previous section circulation around the airfoil generate the necessary lift force required for the insects to fly. So describing ‘Wagner effect’ in terms of circulation around an airfoil helps in understanding the consequences of this effect. As an inclined wing starts impulsively from rest, the circulation around it takes some time to attain a steady-state value. Therefore as shown in the *Figure 5* [19], [20] any wing must travel several chord-lengths before

steady-state circulation is reached. However, the experiments of [20] showed that the delay in lift generation is less noticeable at lower Reynolds numbers.

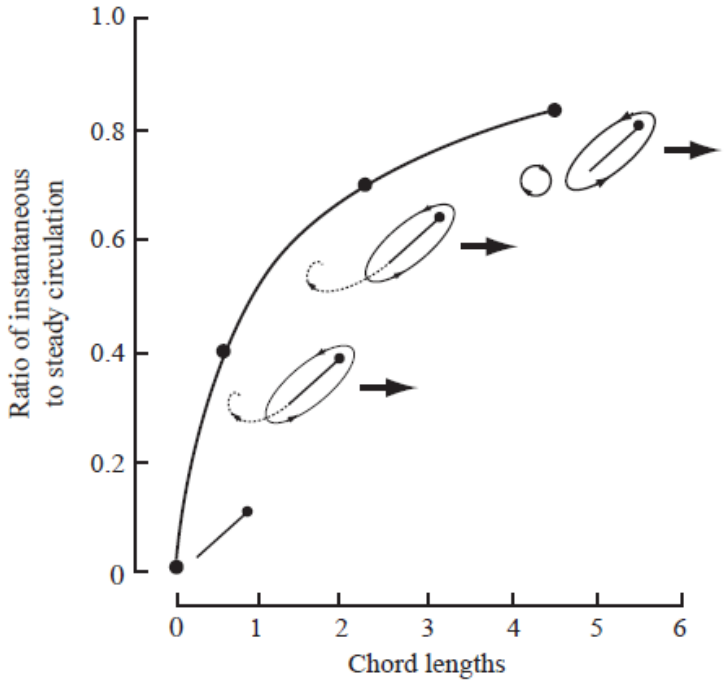

Figure 5: Wagner effect: Plot showing ratio of instantaneous to steady circulation versus chord lengths. Dotted line indicates the formation of starting vortex (trailing edge vortex). As the trailing edge vortex sheds, circulation is build up on the wing section. As stated, a flapping wing travels several chord-lengths before reaching steady-state circulation [19].

2.3.2.3. Delayed stall

In a 2D study, the wings generate an attached leading edge vortex at higher angle of attach. However, if the wings continue to translate at these high angles, the separation of the leading edge vortex takes place. This result in creating trailing edge vortex (from Kutta condition) thereby decreasing the lift force generation. At this stage, the wings are said to be stalled. While before stalling, the wings generate high lift coefficient due to stronger leading edge formation. This development is termed as “delayed stall”.

2.3.3. Wing morphology

Different insects have different wing structure, shape, size and weight. These parameters were observed to increase with their body length. However, not all the wings looks alike. Some insect wings have a complete solid wing while some insects have fringes or hair like structures attached to them. Each of them have their own advantages. Bristles on insect wings serve in different ways 1) They reduce the weight of the wing thereby providing aerodynamic benefit. [8]–[10] , 2) Help to fold and unfold the wings easily [28], 3) Could help in sensing the surrounding fluid and adjust their flight accordingly.

2.4. Large vs tiny insects

Many researchers have presented the complex nature involved in kinematics and aerodynamics of insect flight ranging from *Drasophila* to *Manduca* ([3], [6], [30]), while the studies on tiny insects like thrips, fairy flies, parasitoid wasps are not well explored. Insects like fruit flys and hawk moth fly at *Re* range from about 100 to 10000, while the tiny insects fly at *Re* in the order of 10. In fact, the wing span of the insects can help in determining the *Re* at which its wings operate.

One of the main purposes of an insect during its flight is lift augmentation. Previous works have shown that for most of the mechanisms, predominant lift augmentation is observed in insects at higher angles of attack ([6], [8]). While at theses high angles of attack, leading edge vortices was observed to stick on the top surfaces and remains attached until stroke reversal. It is thought that formation of stable leading edge vortices would be the reason for lift augmentation in insects at high angles of attack. In addition, many researchers has identified that the flight kinematics and aerodynamics of small insects may be different from larger insects ([8], [17], [31], [32]). At low *Re*, drag forces substantially peak, hindering aerodynamic performance of the insects ([31], [32]).

Filming the flight of free-flying insects is a difficult task due to their small size and high wing beat frequency. Though with the availability of high-speed video camera equipped with macro lens, we have very narrow field of view. Hence, very few video recordings of tiny insects are available to date but these recording have provided lot of information regarding the flight of tiny insects. Most of the insects, in fact all the tiny insects that are filmed were observed to use clap and fling mechanism to fly.

A vast amount of research has been carried out on aerodynamics of these insects during clap and fling motion but comparatively most of them were concentrated on larger scale insects ([3], [5], [7], [26], [33]–[35]). Although handful of research was done on the tiny insects like thrips ([28], [36]) there is lot more to understand. It was reported that there are over 5000 different species of thrips alone ([17], [28], [37]). From the snapshots taken during free take off flight of thrips [8], it was observed that they flap their wings at about 200 Hz and their wingspan is as low as 0.5 mm. It was also observed that the wings of many of these tiny insects have fringes or bristles attached to a solid membrane rather than complete solid wing *Figure 6B*. The aerodynamics benefits behind the use of bristled wings were not clear exactly. However, Sunada and others [9] constructed a dynamically scaled bristled wing model and tested them under pure translation and rotation motion. Results show that lift and drag forces are scaled automatically and they did not find any aerodynamic benefit with single wing kinematics. While computational study on bristled wing models during wing-wing interaction showed that the force required to fling the wing apart or clap the wings together decreases [10]. But the limitations on this steady is the assumption of 2D flow around the airfoil which is not true in real conditions.

CHAPTER III

METHODS

3.1. Wing morphology

In this study, we examined forewing morphology 70 species in the order Thysanoptera from published images of insect wings. Thysanoptera (of which thrips is one specific genus) consists of small insects that are 1 mm or less in body length with fringed wings. As a large number of these published images did not have a scale bar to interpret the physical dimensions of the forewing, we acquired measurements of the following geometric variables in pixels: spacing or gap between bristles (G) and diameter of the bristles (D). We also measured the wing length from scale bar information where it was available. From the above measurements, we calculated the dimensionless mean gap to diameter ratio (G/D). We used the following criteria for standardizing the selection of forewing images from published literature: (a) minimum 4 pixels resolution of bristle diameter (at the base of a bristle), (b) good resolution images with scale bars were preferred. We limited our study to one order of tiny insects (Thysanoptera) for the following reasons: (1) thousands of Thysanoptera species have been identified to date, and (2) there has not been a previous effort documenting the range of variation in the geometric design of their bristled wings, in contrast to a recent study examining G/D in the bristled wings of fairyflies (family Mymaridae) belonging to the order Hymenoptera [10].

3.1.1. Morphological measurements

The bristled forewing images of 70 species of thrips (order: Thysanoptera) were analyzed using the public domain image-processing program ImageJ (National Institutes of Health, Bethesda, MD) [38]. For the bristled wing images without a scale bar, measurements were performed in pixels. The inclusion criteria described in previous subsection 3.1 was used to select images for analysis. The diameter (D) and gap (G) between the bristles were measured at the base of the forewing in terms of number of pixels (*Figure 6*). The non-dimensional gap to diameter (G/D) ratio calculated from these measurements was independent of the number of pixels. The gap to diameter (G/D) ratios reported in this study were obtained by averaging G/D values measured along the base of the entire forewing (including the top, bottom and tip of the forewing).

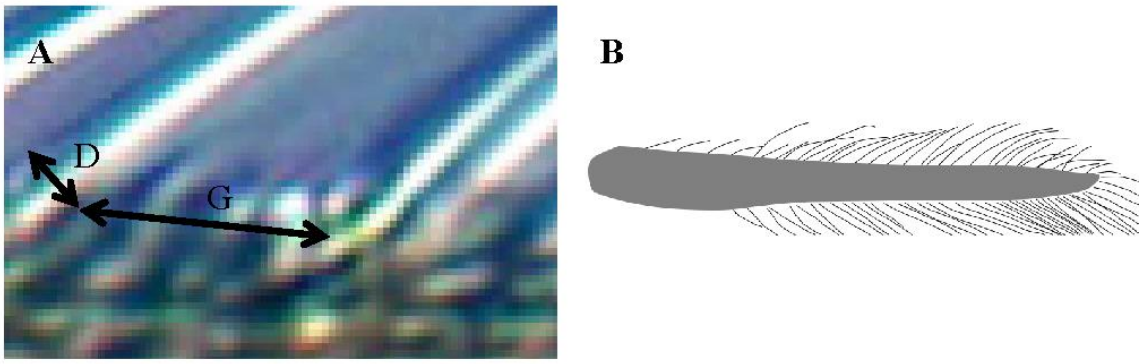

Figure 6: Wing Morphology: A) The bristle diameter (D) and gap between pair of bristles (G) were measured for 70 species of *Thysanoptera* order using ImageJ software. B) Sketch showing the forewing of *Pandanothrips ryukyuensis*. [39]

3.2. Dynamically scaled robotic model

The model used for replicating 'clap and fling' wing-wing interaction (*Figure 7*) consists of two wings that were programmed to move symmetrically in opposite directions. Translation and rotation of each wing was achieved using two programmable 2-phase hybrid stepper motors with integrated encoders (model ST234E, National Instruments Corporation, Austin, TX). Each pair of

rotational and translational stepper motors were rigidly mounted onto an aluminum base plate, which in turn was allowed to slide with minimal friction within two T-slotted extrusions (10-series, part number 1010, 80/20 Inc., Columbia City, IN) using bearing pads (part number 6797, 80/20 Inc., Columbia City, IN). Each wing was mounted onto a stainless steel D-profile shaft of diameter 6.35×10^{-3} m (0.25 inch; part number 8632T151, McMaster-Carr Supply Company, Elmhurst, IL) via a custom-made aluminum L-bracket (shown in *Figure 7*). Each D-profile shaft was coupled to one rotational stepper motor using a pair of nylon miter gears (20 degree pressure angle, 24 pitch, 24 teeth, part number 7297K15, McMaster-Carr Supply Company, Elmhurst, IL),

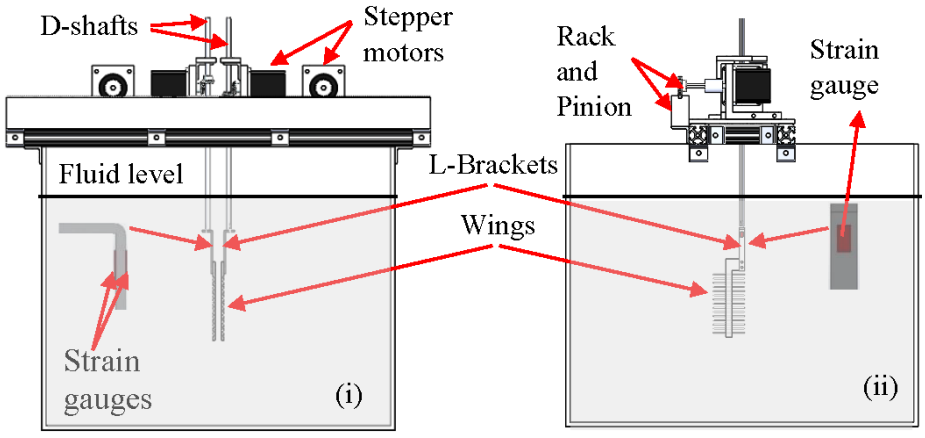

Figure 7: Schematics of experimental setup: (i) front view, (ii) right side view.

for transmitting motion from the rotational stepper motor shaft at a 90-degree angle. Each translational stepper motor was coupled to a nylon pinion gear (14-1/2 degree pressure angle, 32 pitch, 52 teeth, part number 57655K48, McMaster-Carr Supply Company, Elmhurst, IL) that was in turn coupled to a 0.30 m (1-foot) long nylon rack (14-1/2 degree pressure angle, 32 pitch, part number 57655K62, McMaster-Carr Supply Company, Elmhurst, IL). The rack for each translational stepper motor was rigidly mounted onto an aluminum bar that was coupled to the T-slotted extrusion. Each of the two D-profile shafts passed through the aluminum base plate and

was supported by a steel ball bearing (part number 4262T15, McMaster-Carr Supply Company, Elmhurst, IL) that was press-fitted onto the aluminum base plate. All these motors were controlled using a multi-axis motion controller (PCI -7350, National Instruments Corporation, Austin, Texas) via a custom program in LabVIEW software (National Instruments Corporation, Austin, TX). One revolution of each stepper motor was divided into 20,000 steps using a stepper motor drive (model SMD-7611, National Instruments Corporation, Austin, TX). The entire assembly was mounted on the top of a 10.6 x 10^{-2} m^3 (28 US gallons) commercial acrylic aquarium tank (GlassCages.com LLC, Dickson, TN). The aquarium tank had a square cross-section of 0.51 m x 0.51 m (20 inches x 20 inches) and was 0.41 m (16 inches) tall, and was filled with 99% glycerin such that the wings were completely immersed in the fluid medium.

3.3. Physical models

Physical models of solid and bristled wings were fabricated using a 3.17 x 10^{-3} m thick polycarbonate sheet, such that the model wings had a rectangular cross section with 90 x10^{-3} m span and 45 x 10^{-3} m chord length (*Figure 8*). Our model wings were thus nearly two orders of magnitude larger than the typical length scales of tiny insect wings (wing lengths ~ 0.5x10^{-3} m). Bristled wings were fabricated using a 3.17 x 10^{-3} m thick polycarbonate membrane (width, S=8.5 x 10^{-3} m; span=90 x 10^{-3} m) that was surrounded on either side by cylindrical glass rods of 1.00 x 10^{-3} m (1 mm) in diameter to represent bristles. Chord length for bristled wings are measured from one bristle tip to the opposing bristle tip on the other side of the solid acrylic membrane(*Figure 8*). The wing models were tested using the dynamically scaled clap and fling robotic platform for measurements of aerodynamic forces and visualization of flow structures. For specific aim 1, we tested two different wing designs, a solid and a bristled wing of G/D=17, as shown in *Figure 8(A,B)*. For both specific aims 1 and 2, the chord (C) and span of the solid and bristled wings were unchanged. For specific aim 2, we designed two bristled wing models (G/D of 5 and 11) based on morphological analysis of thrips wings and compared the results with the

solid and bristled wing models examined in specific aim 1*(see Figure 8(B, C, D, E))*. The overall dimensions for the modeled wings are shown in *Figure 8 (A, B, C, D)*, where `G' represents the gap between pair of bristles (does not exist for solid), `D' is the diameter of a bristle (does not exist for solid), `S' is the span of the wing, `C' is the chord of the wing, `*s*' is the width of solid membrane (equals chord length (C) in case of solid wing). Bristled wings tested in this study varied in terms of the gap to diameter (G/D) ratio (5, 11 and 17), which is defined as ratio of gap between pair of bristles (G) to diameter of the bristle (D). To facilitate comparison between wing designs, the number of bristles on the bristled wing models were varied while maintain the chord

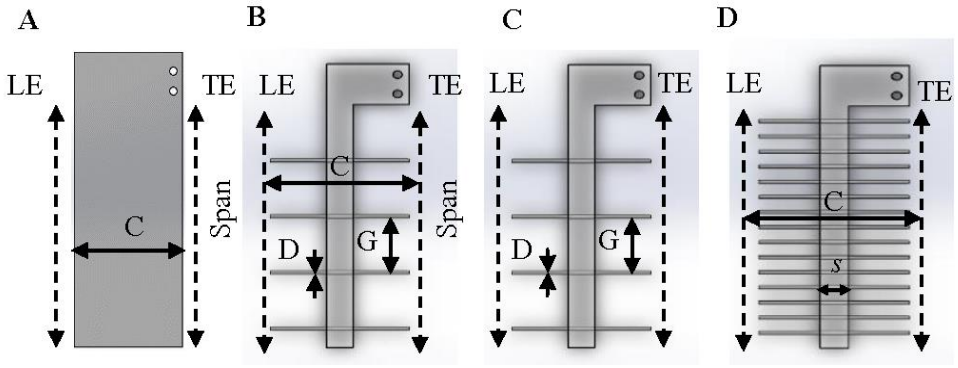

Figure 8: Physical wing models shown with increasing G/D (A) Solid (G/D=0), B) G/D =5, C) G/D =11, D) G/D =17), *s* = 8.5 mm, C = 45 mm, span = 90 mm, D ~ 1 mm, TE = Trailing edge, LE = leading edge.

and span of the wing constant. Chord and span lengths were selected based on dual considerations of: minimizing the influence of tank walls on the flow generated by wing motion, and magnification necessary for imaging studies.

3.4. Kinematics

Our focus in both the studies was to quantify forces and flow structures during 'clap and fling' wing-wing interaction. We did not consider the following portions of wing kinematics seen in flapping flight of insects [19]: (a) flapping translation, and (b) stroke reversal. From previous

studies [19], it was observed that insects maximize their lift force generation using clap and fling mechanism. We used the kinematics examined in a 2D computational study on clap and fling mechanism by [40] to develop motion profiles for the stepper motors in the robotic platform. The motion profile for the stepper motors (velocity in terms of steps/second) was obtained from the variation of non dimensional velocity with non-dimensional time during clap and fling phases (*Figure 9*; redrawn from [40]). The sinusoidal curve represents the rotational motion of one wing while the trapezoidal curve represents the translational motion of one wing. The motion profiles for the 2nd wing was made identical to the first wing, but the motion was set in opposite directional sense with respect to the 1st wing. *Figure 9* shows overlap in translational and rotational motion during both clap and fling phases. During the clap phase, the wings were made to translate along with rotational motion (100% overlap) while during fling phase the wings start to translate after 50% of fling time (50% overlap). The maximum angle of rotation for both clap and fling was 45˚.

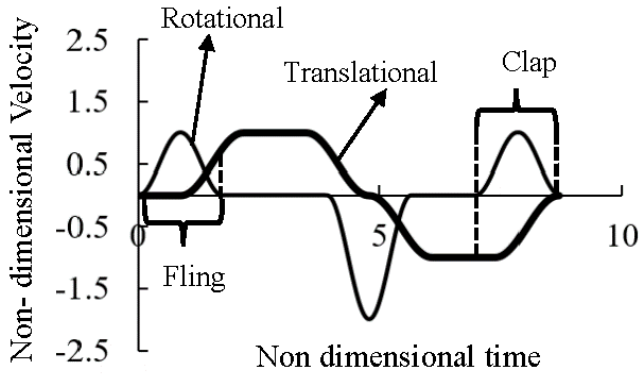

Figure 9: Variation of non-dimensional velocity as a function of non-dimensional stroke time [40]- Solid thick line indicates translational motion while thin line indicates rotational motion of the wing.

The translational velocities were described using a set of equations for acceleration and deceleration phase (taken from [40]). Translation velocity $v(\tau)$ during acceleration phase was given by equations (1), (2) below

$$v(\tau) = \frac{1}{2}V\left\{1 + \cos\left[\pi + \frac{\pi(\tau-\tau_{accel})}{\Delta\tau_{accel}}\right]\right\} \quad (1)$$

$$\tau = tV/C \quad (2)$$

where V is the maximum translational velocity, *v(τ)* is the translational velocity at dimensionless time τ as defined in equation (3), t is the actual time, C is the chord length of the wing, τ_{accel} is the dimensionless time when translational acceleration begins, and $\Delta\tau_{accel}$ is the dimensionless duration of translational acceleration. After acceleration, the translational velocity of the wing is fixed as V as shown in *Figure 9*. The translational velocities during deceleration is given by equation 3.

$$v(\tau) = V - \frac{1}{2}V\left\{1 + \cos\left[\pi + \frac{\pi(\tau-\tau_{decel})}{\Delta\tau_{decel}}\right]\right\} \quad (3)$$

where τ_{decel} is the dimensionless time when translational deceleration begins, and $\Delta\tau_{decel}$ is the dimensionless duration of translational deceleration. τ_{accel} and τ_{decel} were constants and taken as 0.86, while $\Delta\tau_{accel}$ and $\Delta\tau_{decel}$ are taken as 1.3. For more details please refer [40]

Similarly, the angular velocity during the rotational phase at the end of upstroke is given by

$$\omega(\tau) = \frac{1}{2}\omega_{rot}\left\{1 - \cos\left[2\pi\frac{(\tau-\tau_{turn})}{\Delta\tau_{rot}}\right]\right\} \quad (4)$$

$$\omega_{rot} = \frac{2\Delta\theta V}{\Delta\tau_{rot}} \quad (5)$$

where ω_{rot} is a constant determined by the total angle of rotation and by the duration of the rotational phase in equation (5). *ω(τ)* is the angular velocity as a function of dimensionless time, τ_{turn} is the dimensionless time wing rotation begins, $\Delta\tau_{rot}$ is the dimensionless duration of the

rotational phase, and $\Delta\theta$ is the total angle through which rotation occurs. $\Delta\theta$ was set to $\pi/4$ and $\Delta\tau_{rot}$ was set to 1.74. Similarly equation (4), (5) were used for rotational phase at the start of downstroke. Please refer [40] for more details.

3.5. Test conditions

Dynamically scaled robotic model designed to mimic clap and fling motion was used to test each wing model under varying Reynolds number Re_c based on chord length (C). The equation used for Re_c is given by:

$$Re_c = \frac{\rho C V}{\mu} \tag{6}$$

where ρ and μ are the density and dynamic viscosity, respectively, of the fluid medium; C is the chord length of the wing; and V is the maximum translational velocity defined in the above section 3.4. V is calculated from the equations above for a particular Re_c and motion profiles were created for clap and fling using the equations (1)-(5). For constant ρ, μ and V, Reynolds number Re_c does not change between wing models as the chord length c is maintained constant. The dynamic viscosity μ and density ρ of the fluid medium were maintained constant throughout all the experiments. The kinematic viscosity of 99% glycerin solution used in this study was measured using Cannon-Fenske routine viscometer (size 400, Cannon Instrument Company, State College, PA) and found to be 790×10^{-6} $m^2.s^{-1}$. The density of 99% glycerin solution was determined to be 1261.5 kg/m3, via the measurement of mass of predetermined volumes of fluid using a standard mass balance (Scout Pro SP401, Ohaus Corporation, Parsippany, NJ). Re_c was varied between tests by only altering the maximum translational velocity (V) (Table *1*). Starting from the non-dimensional velocity versus time plot (*Figure 9*), different rescaling values were used to vary dimensional U to vary Re_c. For specific aim 1, force measurements and flow visualization were conducted for Re_c in the range of 5-15 (Table *1*) on a solid wing and a bristled

wing model of G/D = 17. For specific aim 2, force measurements and flow visualization were carried out for Re_c=10 on 4 wing models (solid wing, bristled wings with G/D=5 and 11).

Re_c	Cycle frequency (f) [Hz]	V [cm/s]	Clap/Fling time [ms]	Cut-off frequency [Hz]	Frame rate [kHz]
5	0.23	9.1	860	12	0.116
8	0.37	14.6	540	19	0.185
10	0.47	18.2	430	23	0.233
12	0.55	21.9	360	28	0.278
15	0.71	27.4	290	35	0.345

.

Table 1: Experimental conditions used for specific aims 1 and 2. Re_c=chord-based Reynolds number; V = maximum translational velocity. Rescaling of non-dimensional motion profiles were performed using the duration of clap or fling during one cycle. Cut-off frequencies used for filtering raw data obtained from strain gauge measurements were varied for every Re_c tested. Frame rate used for time-resolved particle image velocimetry (TR-PIV) measurements at central chordwise plane to obtain data at identical non-dimensional time points (percentage of clap or fling cycle) across every Re_c tested.

3.6. Force measurements

Time varying forces on the wings were measured using uni-axial linear strain gauges of grid size 3.2 mm x 2.50 mm and nominal resistance of 350 ohms (model SGD-3/350-LY13, Omega Engineering, Inc., 800 Connecticut Ave, Suite 5N01, Norwalk, CT 06854). Wings were attached to the D-shaft of the robotic model Two different custom aluminum L-brackets were fabricated for individual/non-simultaneous lift and drag force measurements (*Figure 10*). The thickness of the L-brackets used for drag and lift force measurements were $2x10^{-3}$ m and $1x10^{-3}$ m, respectively. The variation in thicknesses was necessary to resolve the lower values of lift force (in comparison to drag force) expected for low Re_c in the range of 5-15. Strain gauges were mounted on both sides of the L-brackets (*Figure 10*). The surfaces of the L-brackets were smoothened and cleaned thoroughly so that the strain gauges could be bonded to surfaces with

minimal/negligible air gap. Though a model wing pair was driven to mimic 'clap and fling' wing-wing interaction (*Figure 4*), lift and drag forces were measured only on one wing of the pair. This was based on the assumption that lift and drag forces would be identical in magnitude in each wing of the wing pair, as the motion profile used for prescribing motion of both wings was symmetric.

3.6.1. Data acquisition

Time varying lift and drag forces on a single wing were measured using strain gauges as described above. Raw data in the form of analog voltage outputs were acquired using a data acquisition board (model NI USB-6210, National Instruments Corporation, Austin, TX) via a custom acquisition program written in LabView (National Instruments Corporation, Austin, TX). The strain gauge data was acquired at a sampling frequency (f_s) of 100 kHz at all Re_c (5 to 15) across all the wing models (solid wing; bristled wing of G/D =5,11, 17). *Table 1* shows total clap and fling times during a cycle for varying Re_c (ranging from 5 to 15). The number of samples collected during each cycle for a particular Re_c can be determined as the product of f_s and either fling duration or clap duration. Strain gauge data was acquired through the entire clap or fling time for each cycle but only after 10 clap and fling cycles to allow for a periodic steady state. Strain gauge data were collected during clap and fling across continuous cycles. Strain gauge data needed for calculation of lift and drag forces were obtained non-simulatenously (viz., one force component at a time). Further, since every wing pair tested was driven in a continuous manner (effective 'wingbeat' included both clap and fling), strain gauge data for each force component were acquired continuously for 30 cycles of clap and fling. Later, depending upon the clap and fling time (*Table 1*), we separated the data for clap and fling from each data set of 30 cycles. For every set of strain gauge data, we also recorded the angular position of the wing using the integrated encoders housed within the programmable 2- phase hybrid stepper motors (model ST234E, National Instruments Corporation, Austin, TX). For every set of strain data, we also

recorded the voltage signal before the start of wing motion for baseline shift/offset correction purposes.

3.6.2. Calibration

The maximum values for lift and drag forces in terms of voltage were noted from the acquired strain gauge data. After emptying the tank, the L-brackets used for measuring lift and drag forces were individually calibrated using a 'pulley and bucket' setup (*Figure 10*). Weights were added with increments of 10 grams up to 100 grams (e.g., 10 grams, 20 grams, 30 grams, etc.) and then with increments of 50 grams (e.g., 150 grams, 200 grams, 250 grams, etc.) until the maximum value of voltage was reached. Then the weights were removed in decrements of 50 grams up to 100 grams and then in decrements of 10 grams until zero load. The same procedure was repeated for calibrating the strain gauge located on the other side of each L-bracket. One side of the L-

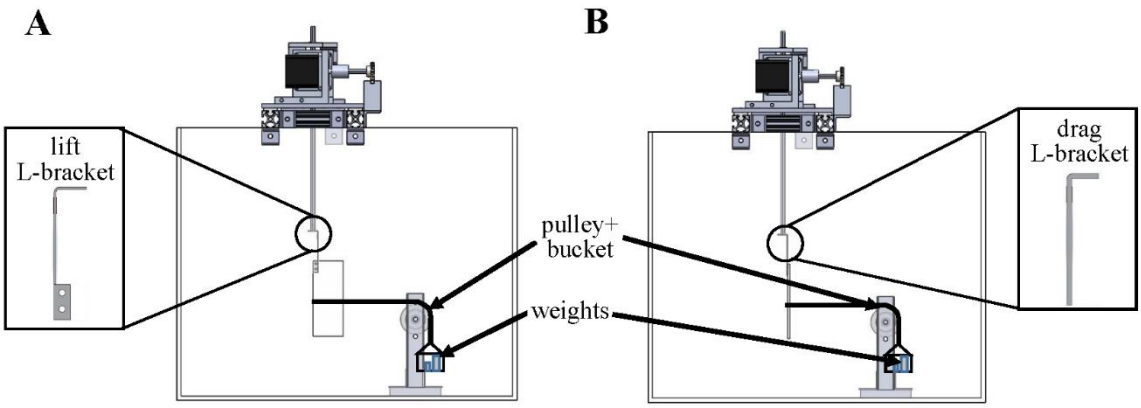

Figure 10: Schematic of strain gauge calibration: (A) setup used for lift L-bracket from left side view; (B) setup used for drag L-bracket from left side view.

bracket provided a voltage signal for a particular load along one direction (e.g., incremented/positive loading) while the other side provided a voltage signal corresponding to loading in the opposite direction (e.g., decremented/negative loading). The measured voltage data (proportional to force component of interest, based on selection of lift or drag L-bracket) were

plotted with respect to the 'true' value (applied weight). Linear regression was performed on the plotted data and a trend line was fitted. The value of slope was calculated from the best-fit linear equation (R2>0.95) corresponding to the trend line (*Figure 11*). This process was performed for both L-brackets (lift and drag) and in both the directions for each bracket. The R2 values (indicative of goodness-of-fit) for lift L-bracket was approximately 0.99 in both directions, while that for drag L-bracket was approximately 0.98 in both directions. The exact list of standard weights used were (in grams): 10, 10, 20, 20, 50, 50, 50, 50, 100. We also calibrated for the weight of the 'bucket' used in calibration setup (2.6 grams) to ensure considering the effects of added mass due to weight of bucket.

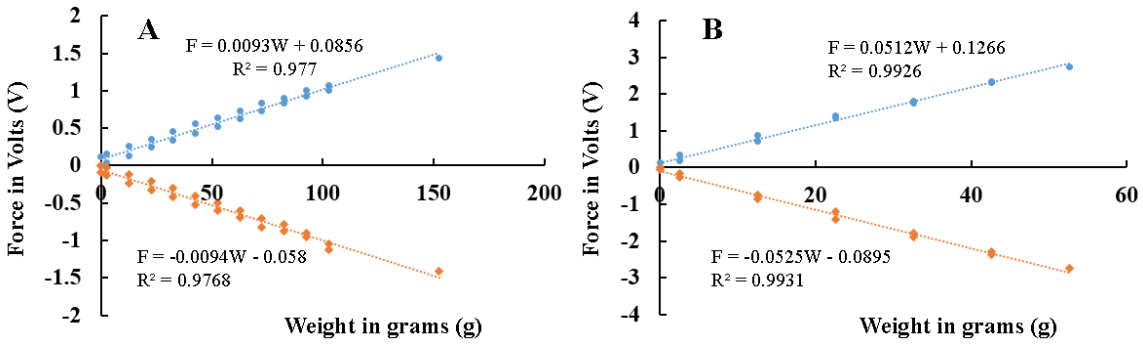

Figure 11: Representative calibration plots for drag and lift L-brackets with weight (W) along x-axis and force (Volts) along y-axis: A) drag L-bracket; B) lift L-bracket.

3.6.3. Processing

Raw force signals in terms of voltage were processed using a custom script written in MATLAB (The Mathworks, Inc., Natick, MA; script included in appendix A.X). The first step in processing was filtering the raw voltage data using a zero-phase delay, third order, low-pass digital Butterworth filter with cutoff frequency varying from 12-35 Hz. The cutoff frequency for a particular Re_c was approximately 10 times of the sampling frequency (f_s) for that specific Re_c, the rationale for which was based on a previous study [6]. *Table 1* presents the cutoff frequency for

filtering at every Re_c tested for both clap and fling time. *Figure 12* shows an example of raw voltage data and its corresponding outcome following filtering.

The second step in processing was cycle-averaging the filtered raw force and angle data across the acquired 30 cycles each of clap and fling, and removing the zero offset by subtracting filtered zero force data from filtered non-zero force data. The third step in processing was to apply the slope obtained from strain gauge calibration to convert the filtered force signal from Volts to N. The choice of using the positive or negative slope obtained from calibration was based on the individual values of uncalibrated, filtered forces (in Volts). For example, if we are applying calibration to drag force at a particular Re_c for any wing model during fling, we first verify each data point of the filtered drag data for positive value and if its true we apply positive drag calibration slope to that data point or else we apply negative drag calibration slope. The fourth step after applying calibration was to calculate non-dimensional coefficients of lift (C_L) and drag (C_D). The equation for calculating C_L, C_D are presented in the below section 3.8.1 (see *equations (7, 8)).*

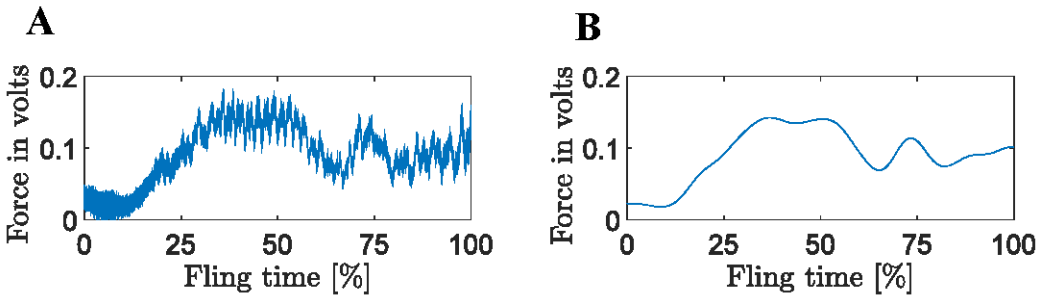

Figure 12: Filtering of strain gauge data: (A) raw lift force data (in Volts) during fling phase at Re_c=10; (B) filtered lift force data (in Volts) for cutoff frequency of 23 Hz.

3.7. Particle Image Velocimetry (PIV)

PIV was used to visualize the flow structures formed along the chordwise (horizontal plane) and spanwise (vertical plane) directions during the wing motion. Chordwise flow field data were used

to determine the strength (circulation) of the leading edge vortex (LEV) and trailing edge vortex (TEV). Spanwise flow visualization data were used to quantify the volume of fluid leaked in between the bristles of bristled wing models.

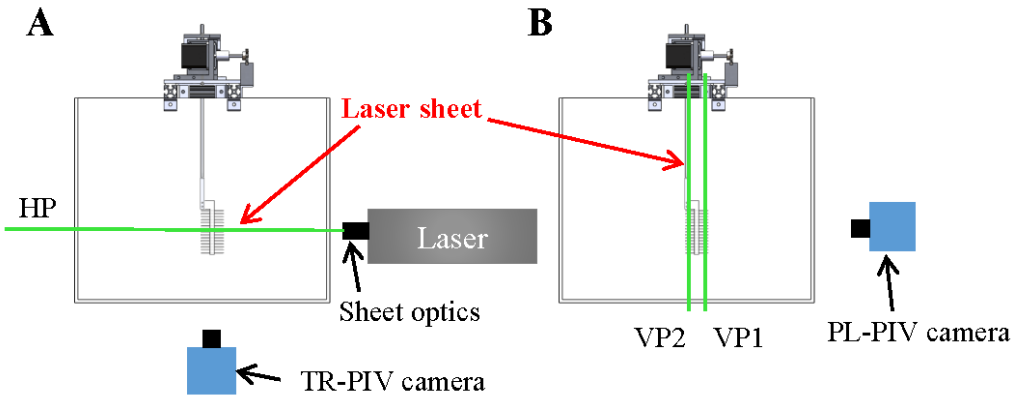

Figure 13: Schematic diagrams showing PIV setup for flow visualization along: (A) chordwise plane illuminated by laser sheet HP; (B) 2 spanwise planes illuminated by laser sheets VP1 and VP2.

3.7.1. PIV along chordwise direction

2D time-resolved PIV (2D TR-PIV) was used to visualize chordwise flow field generated during clap and fling motion of a specific wing pair at a particular Re_c. The schematic for the PIV setup is shown in *Figure 13*. Hollow glass spheres of 10 microns diameter (110P8, LaVision GmbH, Göttingen, Germany) were used as seeding particles in the fluid medium. Seeding particles were mixed in the fluid medium contained in the aquarium tank at least a day before PIV data acquisition to provide adequate time for settling and homogenous initial distribution. One horizontal PIV plane (HP at half the span of the wing) was illuminated using a single cavity Nd:YLF laser (Photonics Industry Inc., NY, USA) that provides a 0.5 mm diameter beam of 527 nm in wavelength. A cylindrical lens (10 mm focal length) was used to make a planar laser sheet from the laser beam. A high-speed 1 MP CMOS camera (Phantom Miro 110, Vision Research

Inc., Wayne, NJ, USA) was positioned at the bottom of the tank and focused onto the seeding particles in the plane HP using a 60 mm constant focal length lens (Nikon Micro Nikkor, Nikon Corporation, Tokyo, Japan). The aperture of the camera lens was set to 2.8 for all experiments. A trigger signal was generated using a custom LabVIEW program at the beginning of clap and fling phases and was provided as an input to the high speed controller unit of the PIV hardware. This trigger enabled the acquisition of PIV data from the same starting point for N cycles each of clap and fling (PIV data for each phase was acquired separately). The PIV particle size was in the range of 1.5-3 pixels. Average particle displacements in the test volume ranged between 4-7 pixels, depending on Re_c. PIV data were acquired for both clap and fling phases across all the conditions tested (varying Re_c and wing model design). For each experiment, 100 raw PIV images per cycle (of either clap or fling) were recorded under varying CMOS camera frame rate based on Re_c, as shown in the *Table 1*. 10 cycles each of clap and fling were recorded separately for each experimental condition (Re_c; wing design).

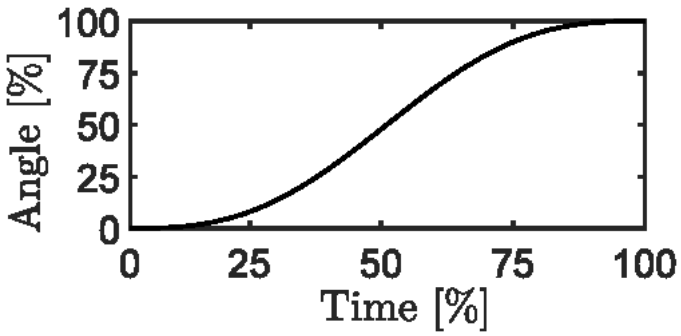

Figure 14: Plot representing % of clap/fling time in terms % of wing rotation.

3.7.2. PIV along spanwise direction

Two-dimensional phase locked particle image velocimetry (2D PL-PIV) was used to visualize flow through the bristles of bristled wing models. The schematic for PL-PIV experimental setup is shown in *Figure 13*. Hollow glass spheres of 8-10 μm diamter (product code 110P8, LaVision

GmbH, Göttingen, Germany) were used as seeding particles in the fluid medium. Two vertical PIV planes (VP1 and VP2 in *Figure 13*) were setup. VP1 is located at approximately 10% of chord length away from the leading edge and VP2 is located at approximately 10% of chord length away from the trailing edge. Each vertical PIV plane was illuminated using a double-pulsed, single-cavity Nd:YAG laser (Gemini 200-15, New Wave Research, Fremont, CA) with wavelength 532 nm, maximum repetition rate of 15 Hz and pulse width in the range of 3-5 ns. The laser beam was converted to a 2D planar sheet of thickness 5 - 6 mm using a cylindrical lens (10mm focal length). A sCMOS camera of spatial resolution 2600 x 2200 pixels, maximum frame rate of 100 fps, and a maximum pixel size of 6.5 μm x 6.5 μm (LaVision Inc., Ypsilanti, MI) was used for recording raw PL-PIV image pairs in frame-straddling mode [41]. Seeding particles in the laser sheet plane were focused using a 60mm constant focal length lens (Nikon Micro Nikkor, Nikon Corporation, Tokyo, Japan). The aperture of camera lens was set to 2.8 for all PL-PIV measurements. A trigger signal was generated for PL-PIV using a custom LabVIEW program at the beginning of clap and fling phases and was provided as an input to the programmable timing unit (PTU) of the PIV hardware. The trigger signal was used as a reference to offset PIV image acquisition to occur at selected phase-locked time points for 10 cycles each during clap and fling phases. The PIV particle size was in the range of 1.5-3 pixels. For specific aim 1, the experiments were carried out in the range of Re_c = 5-15 (see *Table 1*) for solid and bristled wing model of G/D 17. Data was collected at 16 different time points defined in terms of percentage of clap or fling cycle duration (fling: 30%, 35%, 45%, 50%, 55%, 65%, 70%, 100% approximately; clap: 0%,30%, 35%, 45%, 50%, 55%, 65%,70% approximately). These time points were selected based on distributing the maximum fling/clap angle into 8 equally spaced angular points (fling: 12.5%, 25%, 37.5%, 50%, 62.5%, 75%, 87.5%, 100%; clap: 0%, 12.5%, 25%, 37.5%, 50%, 62.5%, 75%, 87.5% of clap angle). Similarly, for specific aim 2, the experiments were carried out at Re_c 10 for all the wing models (Solid, G/D of 5,11,17) at 16 time points. The angular points were obtained using the clap/fling kinematics during rotational motion as shown in *Figure 14*.

We used a rotating turn table with 8 equally spaced angular points drilled precisely using milling machines to collect PIV data along span wise direction of the wing at each specified angle (fling: 12.5%, 25%, 37.5%, 50%, 62.5%, 75%, 87.5%, 100%; clap: 0%, 12.5%, 25%, 37.5%, 50%, 62.5%, 75%, 87.5% of clap angle). For every test condition (Re_c/clap/fling/wing model) a set of 10 image pairs (1 image pair per cycle) phase-locked at one time point in clap/fling rotational cycle. Laser pulse separation intervals between the two images in an image pair (dt) was in the range of 2 ms - 9 ms depending on Re_c. Particle displacements within the FOV ranged between 4-7 pixels.

3.7.3. Post processing

Raw data obtained from chordwise and spanwise PIV recordings, in the form of image pairs, were processed using DaVis 8.3.0 software (LaVision GmbH, Göttingen, Germany). No pre-processing of raw PIV images were performed. Multi-pass cross-correlation was performed on the PIV image pairs with an initial window size of 64x64 pixels (2 passes) and a final window size of 32x32 pixels (2 passes) each with 50% overlap. Post-processing was performed by rejecting velocity vectors with peak ratio Q less than 1.2 and interpolation was used to replace empty vectors. The processed velocity vector fields were phase-averaged for 10 cycles of clap/fling. 2D velocity components (u in x-direction and v in y-direction) of flow in the field of view were obtained following cycle-averaging.

3.8. Definitions for Calculated quantities

3.8.1. Coefficients for Lift (C_L) and Drag (C_D)

Lift coefficient (C_L) and drag coefficient (C_D) were used to quantify non-dimensional lift and drag forces, respectively, generated from 'clap and fling' wing-wing interaction and defined as:

$$C_L = \frac{F_L}{\left(\frac{1}{2}\rho \mathrm{v}_{tip,max}{}^2\right)(c.s)} \quad (7)$$

$$C_D = \frac{F_D}{\left(\frac{1}{2}\rho \mathrm{v}_{\mathrm{tip,max}}{}^2\right)(c.s)} \quad (8)$$

Where F_L, F_D represents lift and drag forces, respectively. ρ represents the density of the 99% glycerin solution, $v_{\mathrm{tip,max}}$ represents the tip velocity of the wing. c and s represent the chord and span of the wing, respectively.

3.8.2. Leakiness

Cheer and Koehl [42] defined leakiness (*Le*) as a non-dimensional quantity that can be used to characterize the amount of fluid leakage through bristled appendages. In this study, *Le* was calculated from the spanwise PL-PIV data of bristled wing models and was defined as:

$$Le = \frac{Q_{viscous}}{Q_{ideal}} \quad (9)$$

$\mathrm{Q_{viscous}}$ indicates the volumetric flux calculated from the spanwise PL-PIV data at a particular location shown in the *Figure 15* , $\mathrm{Q_{ideal}}$ indicates the inviscid volumetric flux and was calculated using the equation:

$$Q_{ideal} = (s - nd)V_{tip} \quad (10)$$

Where s represents the span of the wing, n represents the number of bristles in a bristled wing model, d represents the bristle diameter, V_{tip} represents the tip velocity of the wing at a particular time. It is calculated as shown in the *Figure 15(C)*.

Volumetric flux ($Q_{viscous}$) for a bristled wing model was defined as the volumetric flow rate of fluid that leaked through a pair of bristles along the wing span, in the direction opposite to the wing motion. $Q_{viscous}$ was calculated based on Q_{solid} and $Q_{bristled}$ using the equation:

$$Q_{viscous} = Q_{solid} - Q_{bristled} \quad (11)$$

where Q_{solid} is the volumetric flow rate displaced by a solid wing in the direction of wing motion and $Q_{bristled}$ is the volumetric flow rate displaced by a particular bristled wing model in the direction of wing motion.

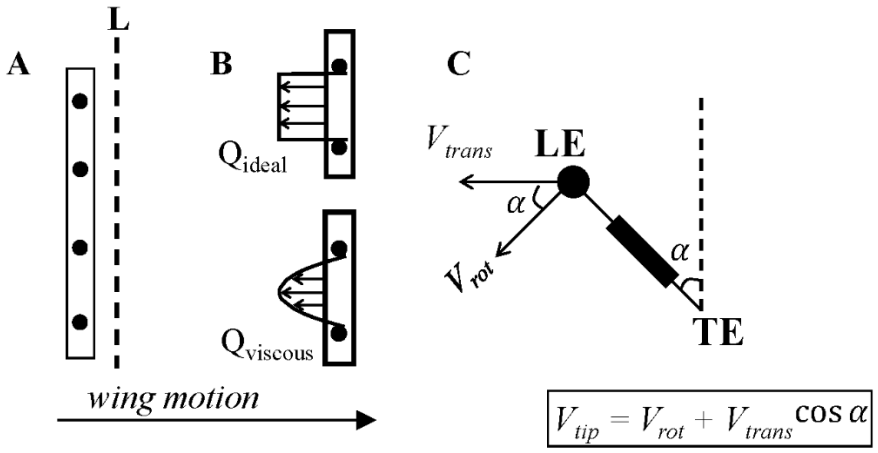

Figure 15: Diagram showing position for volumetric flux calculation for a bristled wing model and leakiness (*Le*) between a pair of bristles under viscous and non-viscous conditions. (A) Bristled wing with the line 'L' representing the position where volumetric flux is calculated, (B) Showing the direction of leakiness with respect to wing motion and leakiness profiles for viscous and non-viscous flows[42]. (C) Showing the calculation for wing tip velocity (V_{tip}) where V_{rot} represents the instantaneous rotational velocity, V_{trans} represents instantaneous translational velocity and α represents the angle made by a single wing at a particular instant.

of wing motion. Both Q_{solid}, $Q_{bristled}$ were calculated at a distance of 5% chord length at a spanwise line 'L' as shown in *Figure 15* using the above equations implemented in a custom MATLAB script.

$$Q = \int_0^L u \, dy \quad (12)$$

Where Q represents Q_{solid} for solid wing model and $Q_{bristled}$ for bristled wing model. u represents the velocity at a distance of 5% chord length at a spanwise line 'L' as shown in *Figure 15*.

3.8.3. Vorticity

The z-component of the vorticity vector (ω_z), indicative of the out-of-plane component, was calculated from the 2D PIV velocity vector field using the following equation:

$$\omega_Z = \frac{\partial v}{\partial x} - \frac{\partial u}{\partial y} \tag{13}$$

where u represents the velocity component along x direction and v represents the velocity component along y direction.

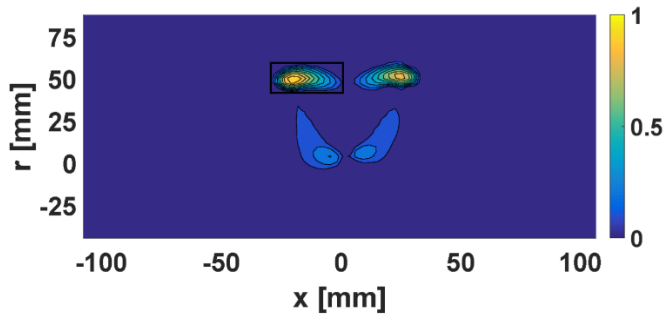

Figure 16: Iso-surfaces of swirling strength λ_{ci} [43] and normalizing them by 4.2% of maximum value ([44], [45]). Stronger LEV and weaker TEV can be observed in this representative image.

3.8.4. Vortex identification and circulation

From 2D TR-PIV along the chordwise plane, we observed the formation of two counter-rotating vortices on each wing. The vortex located near the leading edge of the wing will be referred to as the leading edge vortex (LEV), and the vortex located near the trailing edge will be referred to as the trailing edge vortex (TEV). Vortex identification from the processed PIV velocity vector fields was performed using the swirling strength criterion (λ_{ci}) [43], which is defined as the imaginary part of the complex eigenvalue of the velocity gradient tensor:

$$\lambda_{ci} = Im[eig(\nabla u)] = \frac{1}{2} Im\left(\sqrt{\left(\frac{du}{dx} - \frac{dv}{dy}\right)^2 + 4\frac{du}{dy}.\frac{dv}{dx}}\right) \quad (14)$$

The iso-surfaces of λci were normalized by 4.2% of maximum value as recommended in the previous studies ([44], [45]). To quantify the strength of the LEV and TEV, circulation Γ was calculated by integrating the out-of-plane z-vorticity, ω_z, over the area enclosed by the vortex '*A*' using the equation:

$$\Gamma = \int_A \omega_z dA = \sum_A (\omega_z \; dxdy) \quad (15)$$

A custom MATLAB script was used to calculate LEV and TEV circulation from the chordwise TR-PIV data using the equations (*13*, *14*, *15*), following vortex identification as shown in *Figure 16*.

CHAPTER IV

WING-WING INTERACTIONS WITH VARYING REYNOLDS NUMBER

4.1. Introduction

In this specific aim, a dynamically scaled robotic model was used to conduct force measurements and flow visualization on scale models of one solid wing pair and one bristled wing pair (G/D=17) for Re ranging from 5 to 15. Each wing model was programmed to move following the clap and fling kinematics used in the study by Miller & Peskin (2005) [40]. Lift and drag forces were measured using strain gauges on different L-brackets for lift and drag force measurements during clap and fling phases of wing pair motion. Refer *Figure 2* for wing schematic. Lift was defined as the force in the vertical direction while the drag was defined as the force along the horizontal direction. To visualize flow structures formed in clap and fling motion, we conducted 2D PIV measurements along spanwise and chordwise planes. Chordwise PIV measurements in the solid and bristled wing models at every Re were used to calculate LEV and TEV circulation across clap or fling cycle. The spanwise PIV measurements were used to quantify the proportion of reverse flow through the bristles via leakiness.

Aerodynamic forces were non-dimensionalized to obtain lift and drag coefficients (C_L and C_D). The force coefficients for the solid and bristled wing models were examined as a function of varying percentage of clap or fling cycle time for every Re tested in this aim. Force coefficients for the solid and bristled wing models were compared to the LEV and TEV circulation to examine how lift generation is impacted by the presence of bristles. Leakiness obtained from

spanwise PIV was used to develop a physical explanation for larger drag reduction in bristled wings (relative to lift) undergoing clap and fling interaction.

4.2. Results

4.2.1. Force generation

After processing the strain gauge data for obtaining aerodynamic forces, lift coefficient (C_L) and drag coefficient (C_D) were determined using equations (6) and (7) described previously. The force coefficients were averaged over 30 cycles each of clap and fling phases. In general, lift and drag coefficients were lower for Re_c = 10 as compared to Re_c = 5 for both solid and bristled wings in clap and fling (*Figure 17*, *Figure 18*). This is in agreement with previous observations on force generation in clap and fling at this range of Re_c [8].

Force generation in fling

For a constant Re_c, drag coefficient for the solid wing model peaks close to 50% of the fling time and fluctuates during the rest of fling (*Figure 17*A) These fluctuations may be potentially caused by the overlapping translational motion of the wings that starts from 50% of fling cycle, as seen in the motion profile used to drive wing motion (*Figure 9*). Additionally, the fluctuations observed after peak drag coefficient of the solid wing model tend to smoothen with increase in Re_c.

In contrast to the solid wing, no fluctuations were observed in the time-variation of C_D in the bristled wing (*Figure 17*A). This could be potentially due to flow leaking through the bristles, causing drag force to not fluctuate during overlapping translational motion. Comparing the drag coefficients between solid and bristled wing models, roughly an order of magnitude reduction in C_D was observed for the bristled wing model, suggesting that bristles indeed reduce the forces needed to fling the wings. This is also supported by previous studies ([8], [10]).

While we observed reduction in drag force for the bristled wing as compared to a solid wing, the plots for C_L versus fling time *(Figure 17B)* shows that C_L of both the bristled and solid wings are roughly in the same order of magnitude. Negative lift can be observed for the solid wing model at Re_c = 5 at the start of the fling. A smaller magnitude of negative lift was observed for the solid wing at Re_c=10. In general, negative lift can be expected to be counterproductive to weight support. In contrast, little to no negative lift was observed for the bristled wing model at both Re_c of 5 and 10, showing a modest improvement from the solid wing purely via the inclusion of bristles.

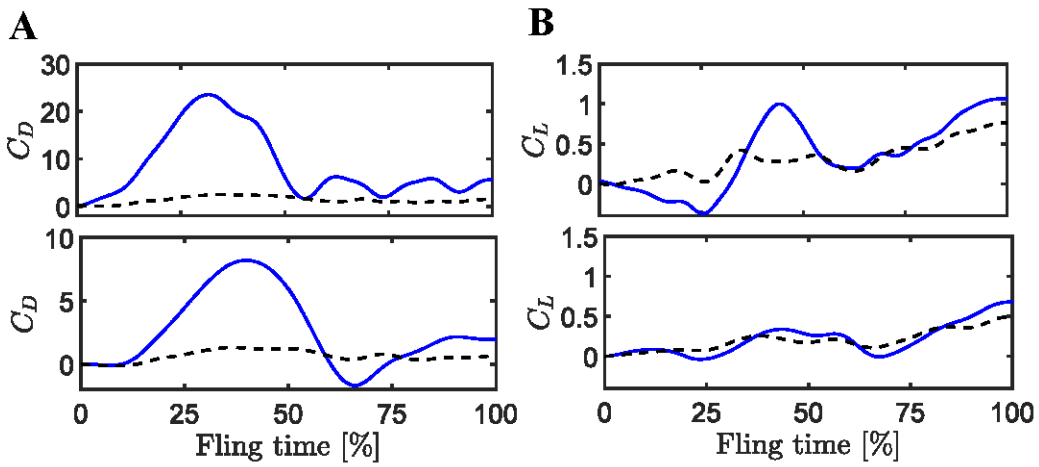

Figure 17: Variation of force coefficients as a function of cycle time for solid wing (——) and bristled wing (– –) pairs during fling. (A) Drag coefficient C_D for Re_c = 5 (top), Re_c = 10 (bottom). (B) Lift coefficient (C_L) for Re_c = 5 (top), Re_c = 10 (bottom).

Force generation in clap

Drag coefficient fluctuates during most of the clap time for solid wing model (*Figure 18*) for solid wing model shows that drag force looks to fluctuate during most of the clap time. As mentioned earlier in the case of fling, these fluctuations during clap phase could be due to overlap of translational motion with wing rotation. In addition an alternative explanation could be due to mechanical vibrations of the wings themselves. Also, these fluctuations dampen with increase in

Re_c. We do not observe fluctuations in C_D for the bristled wing model. This could be potentially due to leakage of flow in between the bristles causing drag force to stabilize during translational motion. Comparing C_D for solid and bristled wing models, we found that the C_D was lower for bristled wing model. However, the magnitude of drag reduction in clap on account of bristled wings was not as large as that observed earlier in fling. In terms of lift force, the lift coefficient C_L was observed to increase for about 50% of the clap time and then start to decrease for remaining time at all Re_c. Comparing C_L under varying Re_c, we observe that C_L decreases substantially with increasing Re_c for the solid wing model. A small reduction in C_L was observed for the bristled wing model when compared to the solid wing model, Further, C_L of the bristled wing model also decreased with increasing Re_c.

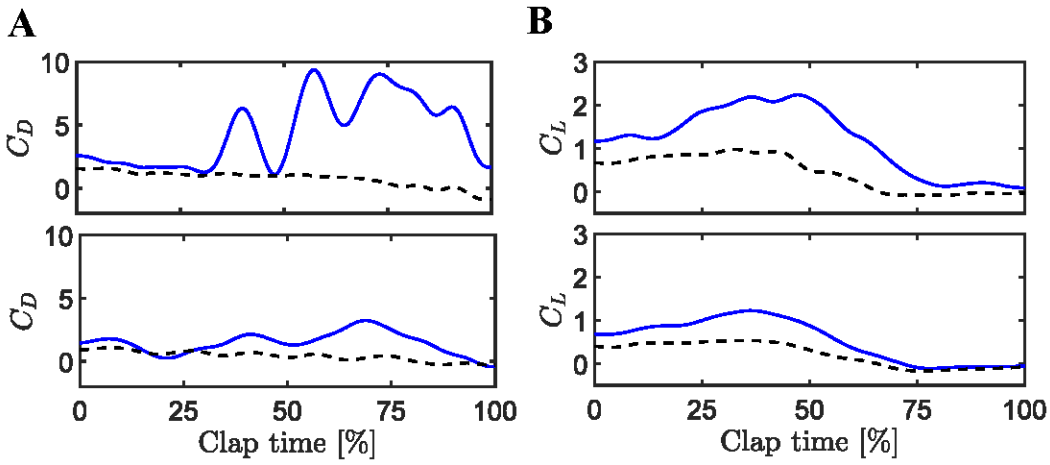

Figure 18: Variation of force coefficients as a function of cycle time for solid wing (——) and bristled wing (– –) pairs during clap. (A) Drag coefficient C_D for Re_c = 5 (top), Re_c = 10 (bottom). (B) Lift coefficient (C_L) for Re_c = 5 (top), Re_c = 10 (bottom).

Peak drag and lift force analysis during clap and fling

Figure 19 shows the Re_c variation of maximum drag coefficient ($C_{D,\max}$), maximum lift coefficient ($C_{L,\max}$) and ratio of maximum lift coefficient over maximum drag coefficient ($C_{L,\max}$ / $C_{D,\max}$) for solid and bristled wing models during clap and fling phases. Both $C_{D,max}$ and $C_{L,max}$ decreased with increasing Re_c, and the decrease in force coefficients was larger for solid wings when compared to bristled wings during both clap and fling phases.

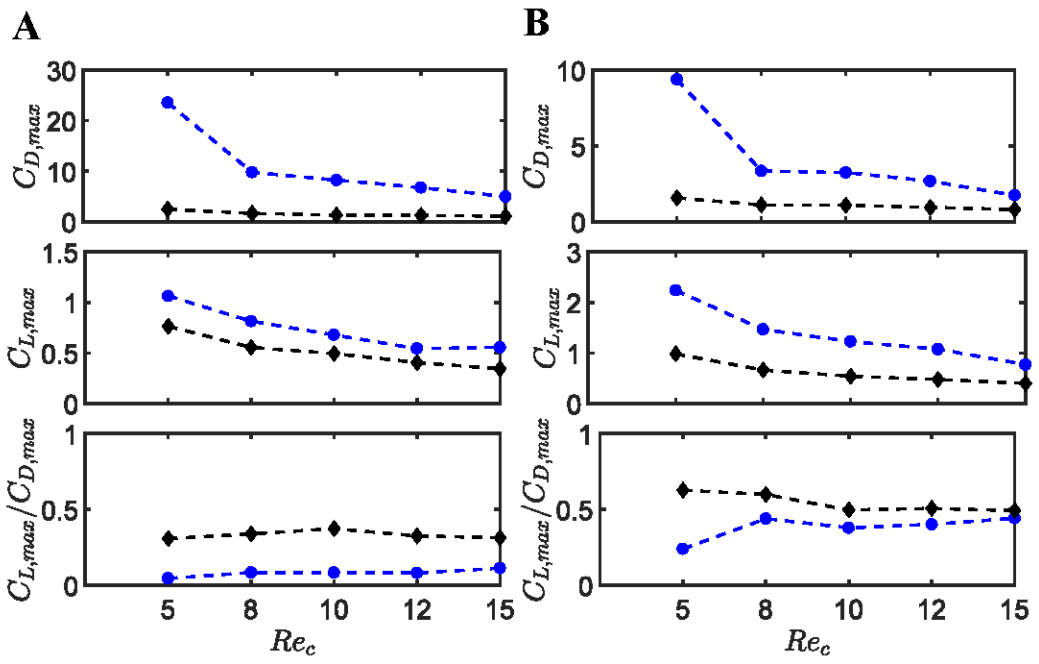

Figure 19: Variation of peak force coefficients and ratio of peak lift coefficient to peak drag coefficient with Re_c for solid (-●-) and bristled (-◆-) wing models. A) fling, and B) clap.

For a particular Re_c in the range of 5 to 15, $C_{D,max}$ and $C_{L,max}$ decreased for the bristled wing when compared to the solid wing, irrespective of clap or fling phase. Also, the decrease in $C_{D,max}$ in the bristled wing model was more compared to decrease in $C_{L,max}$. Consequently, the ratio of maximum lift coefficient to maximum drag coefficient ($C_{L,max}$/ $C_{D,max}$) was largest in the bristled wing model across all Re_c tested during both clap and fling times. Interestingly, $C_{D,max}$ was observed to be nearly invariant with Re_c for bristled wings during both clap and fling phases,

showing the importance of bristles in maintaining a relatively constant drag force across two orders of magnitude of Re_c.

4.2.2. Leakiness

To quantify the flow through the bristles during clap and fling, we calculated leakiness between the bristles from the spanwise PL-PIV measurements for solid and bristled wing models. As detailed in the methods chapter, leakiness (*Le*) was calculated using a custom MATLAB script using equations (*9*)-(*12*). *Figure 20, Figure 22* shows the variation of *Le* in fling and clap cycle times, respectively, across all Re_c tested. In general, *Le* followed the same trend of variation in cycle time irrespective of the particular Re_c condition. In fact, *Le* was observed to only differ marginally across the tested Re_c range.

Leakiness in Fling

While *Le* showed variation between 0.4 to 1 across the fling cycle for any particular Re_c, the time point where maximum leakiness (Le=1) was observed remained invariant with Re_c---corresponding to 37.5% fling angle (≈ 40% of fling time). An examination of how *Le* at this particular time point varies with Re_c *(Figure 20B)* shows that *Le* increases from approximately 0.6 at Re_c=5 and reaches the maximum value of 1 at Re_c=8, after which remains constant under increasing Re_c. This suggests that leaky flow through bristles diminishes at Re_c=5, and provides evidence of a lower limit (Re_c~O(1)) where bristles would not be efficacious in drag reduction. This observation is also supported by the reduced ratio of peak lift to peak drag coefficients for Re_c < 10 (*Figure 19*).

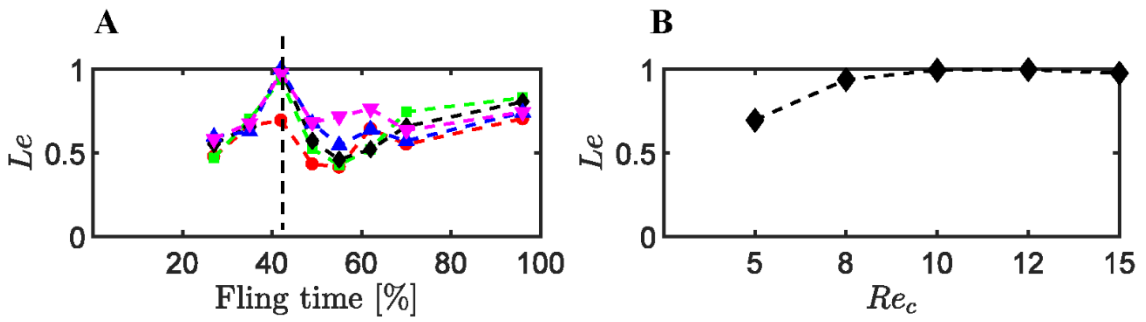

Figure 20: Leakiness (*Le*) as a function of fling time and Re_c. A) Re_c = 5; Re_c = 8; Re_c = 10; Re_c = 12; Re_c = 15. Leakiness was observed to peak at ~40% of fling time (37.5% fling angle) for all Re_c tested. B) Leakiness v/s Re_c at ~40% fling (dashed line in part A).

To visualize the leaky flow through the bristles during fling, we examined the velocity vector fields obtained from spanwise PIV measurements (*Figure 21A*). Small recirculating vortices were observed to form in between the bristles. The peak velocities in these 'leaky vortices' were observed to increase after 37.5% fling angle (≈40% of fling time) and remain mostly constant until 87.5% fling angle. Note that the increased intensity of these recirculating vortices at 40% fling time corresponds to the time point where maximum *Le* was observed across all Re_c *(Figure 20).* We can thus infer that recirculation of leaky flow through the bristles is indeed the reason for increase in *Le* at that time point in fling cycle.

Leakiness in clap

In contrast to *Le* in fling, *Le* in clap was observed to show little variation during clap cycle time for all Re_c tested (*Figure 22*). Further, *Le* values during clap were generally lower when compared to *Le* in fling. This suggests that bristles leak more fluid during fling as compared to clap phase. For comparing how *Le* variation with Re_c differs between fling and clap , we examined *Le* as a function of Re_c at 37.5% of clap angle (~ 40% of clap time). This time point was selected as it corresponded to the time point of maximum *Le* in fling. For the case of clap, *Le*

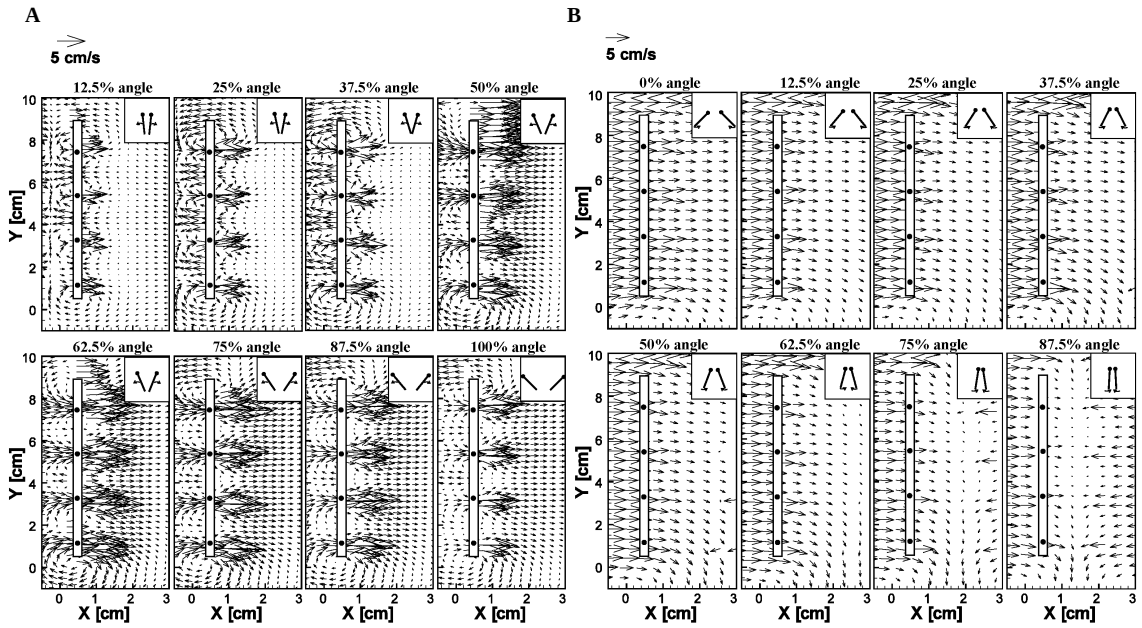

Figure 21: Velocity vector fields describing the flow through the bristles during (A) fling (left) and (B) clap (right) for a bristled wing model (G/D=17) at Re_c=10. In the case of fling, recirculating vortices form in between the bristles at 37.5% of fling angle and eventually dissipate at higher angles. However, recirculating vortices in between the bristles are not observed in clap.

showed only a small variation with Re_c at this time point *Figure 22*. To investigate why leakiness during clap is markedly lower when compared to fling, we examined the velocity vector fields obtained from spanwise PL-PIV (Figure *21B*). In direct contrast to the observation of flow through bristles in fling, 'leaky vortices' were not observed in between bristles. This underscores the importance of these recirculating flow structures in modulating the overall *Le* of a bristled wing. Moreover, the functional implications of these 'leaky vortices' are directly reflected in the extent of drag reduction achievable by a particular bristled wing design in either clap or fling. A comparison of *Figure 17A* and *Figure 18A* (and $C_{D,\max}$ in parts A and B of *Figure 19*) show that drag reduction during clap of a bristled wing pair was lower than that during fling.

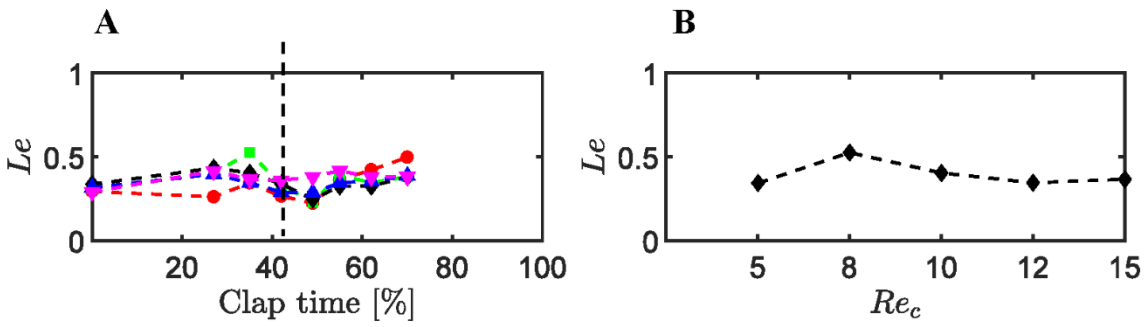

Figure 22: Leakiness (*Le*) as a function of clap time and Re_c. A) Re_c = 5; Re_c = 8; Re_c = 10; Re_c = 12; Re_c = 15. B) Leakiness v/s Re_c at ~40% clap time (dashed line in part A). Leakiness was observed to have little effect with change in Re_c during clap phase.

4.2.3. Circulation

Figure 23 and *Figure 24* show the out-of-plane vorticity (ω_z) contours overlaid on velocity vector fields at Re_c =10 for solid and bristled wing models at 4 time points each of clap and fling (25%, 50%, 75%, 100% of fling angle; 0%, 25%, 50%, 75% of clap angle). These were obtained from 2D TR-PIV measurements acquired at chordwise plane HP (located at mid-span as referred in the *Figure 13*. From the plots (*Figure 23*), with increasing fling angle, we observe the formation of stronger leading edge vortex compared to trailing edge vortex at all time points for two wing models (solid, bristled). With increasing fling angle, we observed the formation of a stronger LEV compared to the TEV at all time points for both the solid and bristled wing models (*Figure 24*). In contrast, we observed the formation of stronger TEV compared to the LEV for both the solid and bristled wing models at all time points during clap (*Figure 24*). In general, both the LEV and TEV were weaker for the bristled wing when compared to those of the solid wing during clap and fling phases.

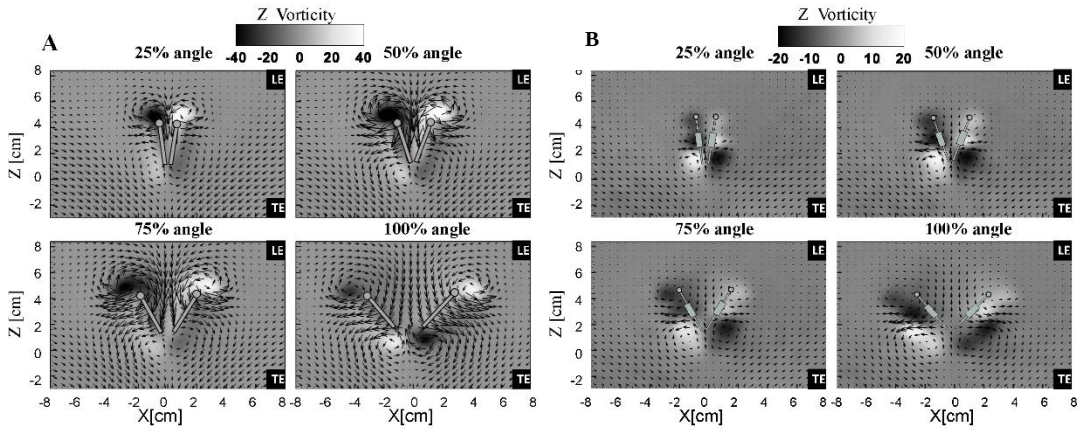

Figure 23: Vector and vorticity plots for solid and bristled wing model during fling at Re_c = 10, A) Solid wing model at 25%, 50%, 75%, 100% fling angle, B) Bristled wing model at 25%, 50%, 75%, 100% fling angle, LE - leading edge, TE - Trailing edge.

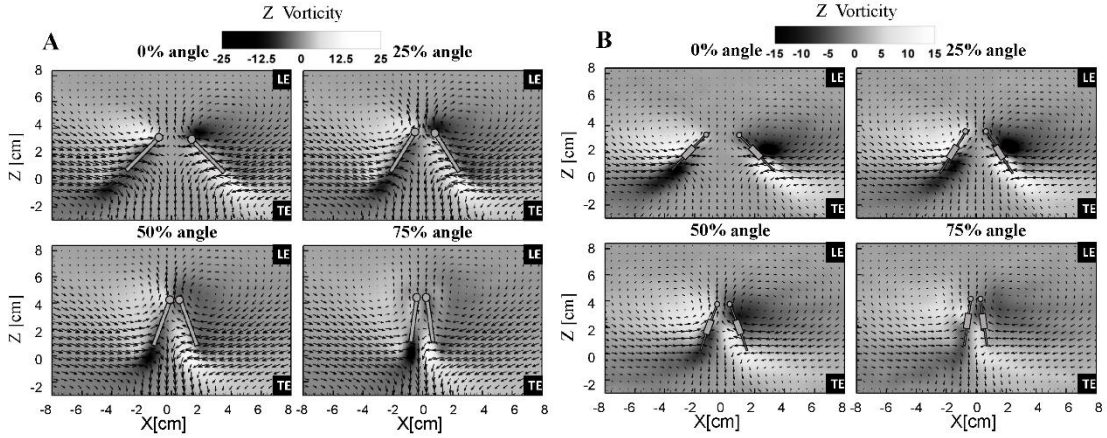

Figure 24: Vector and vorticity plots for solid and bristled wing model during Clap at Re_c = 10, A) Solid wing model at 0%, 25%, 50%, 75% clap angle, B) Bristled wing model at 0%, 25%, 50%, 75% clap angle, LE - leading edge, TE - Trailing edge.

The velocity vectors for bristled wing model were smaller compared to solid wing model at Re_c=10 during clap and fling phases. Since the forces generated by the wings are related to the strength of the LEV and TEV, we calculated circulation of LEV (Γ_{LEV}) and TEV (Γ_{TEV}) from equations (13)-(15) implemented in a custom MATLAB script (*Figure 25*).

During fling, Γ_{LEV} was larger for the solid wing compared to bristled wing, while Γ_{TEV} did not appreciably change between solid and bristled wing models. For the bristled wing model, there is

little change in Γ_{LEV} and Γ_{TEV} throughout the fling cycle at Re_c=10. This was also observed for all other Re_c tested (not shown). Finally, the net circulation (Γ_{Net}), defined as Γ_{Net}=||Γ_{LEV}| - |Γ_{TEV}||, was larger for the solid wing compared to the bristled wing model.

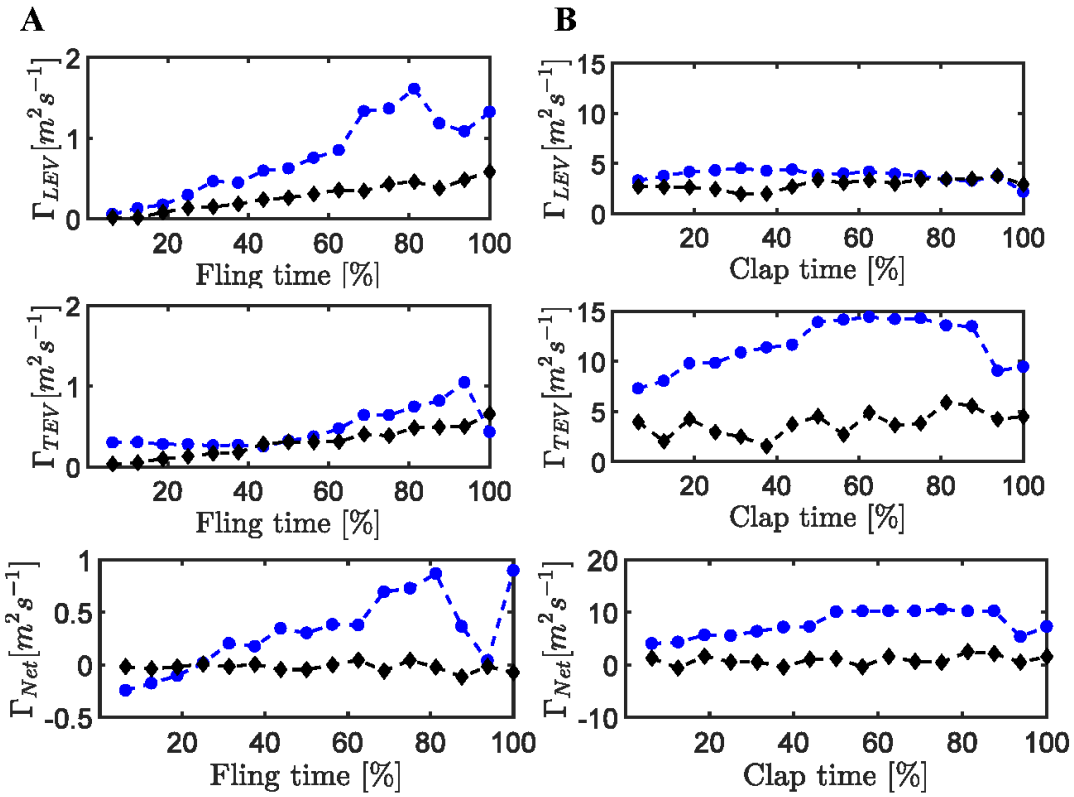

Figure 25: Circulation in fling (A) and clap (B) at Re_c=10. Top: LEV circulation Γ_{LEV}, middle: TEV circulation Γ_{TEV}, and bottom: net circulation Γ_{Net}.

Figure 25B shows the LEV, TEV and net circulation at Re_c = 10 during clap phase. Γ_{TEV} was larger in clap for solid wing compared to bristled wing model, while Γ_{LEV} shows little change between solid and bristled wings. Further, both Γ_{LEV} and Γ_{TEV} do not appreciably change the bristled wing model throughout the entire clap cycle at Re_c = 10. This was consistent with other Re_c tested (not shown). Finally, the net circulation (Γ_{Net}) in clap was larger for solid wing compared to bristled wing model.

4.3. Discussion

In this study, we observed the following: (1) during wing-wing interaction, both lift and drag coefficients were lowered in the case of bristled wings when compared to those of solid wings across both clap and fling phases at the range of low Re_c tested in this study; (2) the reduction in C_D for bristled wing as compared to a solid wing was disproportionally larger when compared to reduction in C_L between bristled and solid wings during both clap and fling phases; (3) peak lift over peak drag ($C_{L,max}$ /$C_{D,\,max}$) was largest for bristled wings compared to solid wings across the entire range of Re_c from 5 to 15; (4) leakiness was markedly elevated during the entire fling phase as compared to clap, supporting the above observation that bristles primarily reduce the force required to fling the wings apart. From the above findings, we propose that clap and fling interaction with bristled wings provides unique benefits over solid wings in terms of augmenting the overall aerodynamic efficiency of flapping flight.

A previous experimental study using scale models of bristled wings [9] found that forces acting on single bristled wing models undergoing translation and rotation were lower when compared to equivalent single solid wing models. This is also supported by our findings. However, our study shows that wing-wing interaction can enhance the aerodynamic efficiency when using bristled wings. A recent 2D computational study on bristles wings proposed that there was substantial decrease in force required to peel the wings apart at low Re_c relevant to tiny insect flight [10]. From our results, we observed that C_D decreased significantly for bristled wings over a range of Re_c. Another previous study that approximated the bristled structures as porous wings [8] showed small augmentation in aerodynamic efficiency over a range of low Re_c in wing-wing interaction as opposed to single wing translation, which supports our finding that bristled wings can provide aerodynamic benefits over solid wings specifically during wing-wing interaction.

From our findings, we noticed that both C_L and C_D decrease for bristled wings during clap and fling phases. But a disproportionally larger drop in C_D as compared to C_L allowed for an overall increase in C_L/C_D. We also observed that the ratio of maximum lift coefficient ($C_{L,max}$) to maximum drag coefficient ($C_{D,max}$) increased from solid to bristled wing at a given Re_c during both clap and fling motion. To understand the physical mechanicsm responsible for this disproportionate reduction in C_D as compared to C_L, we examined flow through the bristles and quantified leakiness as well as the circulation of LEV and TEV for all wing models.

Chordwise PIV results during fling show that LEV circulation (Γ_{LEV}) was larger for solid compared to bristled wing model. In contrast, Γ_{LEV} did not change appreciably between solid and bristled wing models during clap phase. During fling, TEV circulation (Γ_{TEV}) did not change much between solid and bristled wing model whereas Γ_{TEV} was larger for solid wing in clap phase as compared to the bristled wing. Hence, the net circulation (Γ_{Net}) decreased in bristled wing model when compared to solid wing for both clap and fling motion. From the work of Wu (1981), net circulation can be understood as being directly proportional to lift force (i.e. lift coefficient $C_L \propto \Gamma_{Net}$). Therefore, a decrease in Γ_{Net} would imply a decrease in C_L. Hence, when moving from a solid to a bristled wing, C_L would decrease during both clap and fling.

For the solid wing model, leakiness (*Le*) can be defined to be zero. *Le* was observed to increase in the bristled wing model during both clap and fling. Drag force generated by a wing model is a measure of reaction force of the fluid surrounding the wing in direction of motion (horizontal direction as defined in our study). If the wing were designed such that fluid could leak through the span, then the reaction force experienced by the fluid in the direction of motion would decrease. Hence, drag force reduction can be explained by an increase in *Le.* We observed that the bristled wing model leakiness fluctuated largely during fling, reaching its maximum possible value of 1 in fling at approximately 40% of fling cycle time at all Re_c. This implies that almost all the fluid surrounding the wing was being leaked through the bristles. For the first time, we

examined the flow through the bristles (a factor that has not been examined in previous studies on bristled wings) and observed the formation of 'leaky vortices' or recirculating flow structures around the bristles *Figure 23*. These vortices provided the observed larger reduction in drag force in the bristled wing model. During clap phase, *Le* was observed to not reach the maximum value of 1, and this was reflected in a smaller extent of C_D reduction in clap phase (between solid and bristled wings) as opposed to fling.

In both clap and fling, we observed that there was small reduction of C_L from solid to bristled wing model and a larger reduction in C_D. Thus, the ratio C_L/C_D can be expected to increase for the bristled wing model as compared to the solid wing, also seen in the force ratio results presented here ($C_{L,max}/C_{D,max}$). This unique role in augmenting aerodynamic efficiency could explain why the smallest flying insects use bristled wings. In addition, bristles would reduce the overall wing weight, which lowers the magnitude of lift force needed for weight support.

CHAPTER V

WING-WING INTERACTIONS WITH VARYING G/D RATIO

5.1. Introduction

For specific aim 2, we used the same dynamically scaled robotic model as in specific aim 1 for determining the aerodynamic forces acting on bristled wing pairs with different gap to diameter (G/D) ratios during clap and fling phases. The kinematics and the procedures used for obtaining the force and particle image velocimetry (PIV) data were the same as in specific aim 1 (see methods chapter). In specific aim 2, we collected morphological data of spacing between bristles (G) and bristled diameter (D) from analysis of published thrips forewing images. Using this morphological data, we designed and developed two physical models of bristled wing pairs (G/D of 5 and 11) for testing in the robotic clap and fling model. To investigate the fluid dynamic mechanism underlying variation in aerodynamic forces with G/D ratio, we also examined both spanwise and chordwise flow fields using PIV. Aerodynamic force coefficients, leakiness of flow through bristles, and circulation (strength) of the leading edge vortex (LEV) and trailing edge vortex (TEV) were comparatively examined under varying G/D for a single value of chord-based Reynolds number (Re_c) of 10.

5.2. Results

5.2.1. Wing morphology

Forewing images in 70 species of thrips (order: Thysanoptera) were analyzed using ImageJ open

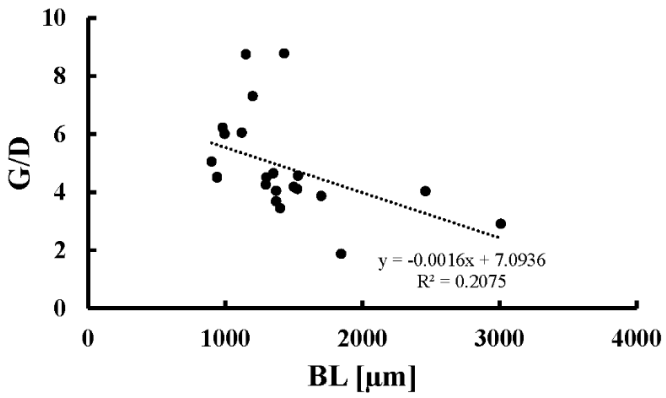

Figure 26: Variation of gap to diameter ratio (G/D) in forewing of 23 species of thrips as a function of body length (BL) in µm. G/D was observed to generally decrease with increase in BL, However, there was no correlation between G/D and BL among these 23 species (see table 2).

Species Name	G/D	Body Length (BL) [µm]
T. alavii	5.37	-
P. albipennis	3.38	-
H. aliceae	3.69	1370
H. ananthakrishnani	8.85	-
H. argenticinctus	3.5	-
N. asiaticus	4.25	-
B. borealis	5.23	-
E. bagnall	5.75	-
S. balteus	4.53	940
N. basilaris	4.1	-
F. basseti	2.05	-
H. bicinctus	9.32	-
S. biformis	7.75	-
B. borealis.	4.05	1370
F. brunneicornis	4.03	2460
N. burungae	4.63	-
F. caseariae	5	-
T. clarisetis	2.63	-
N. clavisetis	6.22	980
L. daedali	3.8	-
M. distalis	4.71	-
P. dracaenae	5.94	-
F. fuscicornis	5.2	-
F. minuta	5.5	-
F. occidentalis	4.45	-
F. peruviana	4.73	-
C. fasciatus	8.46	-
N. gracilipes	11.46	-
L. guaraniticus	7.31	1200
H. dissociatus	3.87	1700
H. reuteri	3.82	-
N. hadrosetae	7.7	-
H. haschemi	4.81	-
H. herajius	1.87	1845
S. hullikali	7.87	-

Species Name	G/D	Body Length (BL) [µm]
C. idrisi	4.65	1350
T. inconsequens	3.22	-
A. iotus	4.11	1525
K. katarinae	3.45	1400
L. kaminskii	4.51	1300
S. langkawiensis	8.75	1150
A. longistylus	6.52	-
H. marginatus	1.83	-
D. marissae	5.05	900
T. meridionalis	3.93	-
N. bellisi	6.74	-
N. new species	3.3	-
A. navsariensis	5.07	-
Neohydatothrips haydni	4.32	-
N. notialis	6.01	995
C. octarticulatus	11.94	-
Ch.orchidii	6.2	-
F. orizabensis	2.17	-
N. paraensis	6.38	-
T. parvispinus	9.95	-
T. razanii	8.78	1430
N. renatae	4.5	940
S. rubrocinctus	7.39	-
P. ryukyuensis	4.57	1530
S. sexmaculatus	4.23	-
S. szitas	3.77	-
S. spinalis	5.75	-
F. strasseni	2.91	3010
T. alliorum	4.18	-
T. meruensis holmi	4.89	-
Thripinae Euphysothrips	7.34	-
L. vaneeckei	2.99	-
F. veracrucensis	4.26	1295
P. wangi	6.05	1120
Y. yangtzei	4.18	1500

Table 2: Thrips species (n=70) considered for morphological analysis and calculated G/D. BL indicated wherever available. BL=body length; G/D=gap to diameter ratio.

source software [38]. Not all the images analyzed included scale bars or information in the text on body length (BL). We found 23 species for which BL was reported, most of which ranged in BL from 900 µm to 1700 µm. For species with reported BL, we calculated G/D using the procedure specified in the methods section and plotted G/D ratio with varying BL (Figure *26*).

Linear regression showed that G/D ratio generally decreased with increase in BL. However, there was no correlation between G/D and BL. *Table 2* shows the species analyzed, BL and G/D values. Statistics for G/D variation from all of the thrips forewing images that were analyzed (70 species) are shown in Table *3*.

	Minimum	Maximum	Mean	Median	Standard Devation
G/D	1.82	11.9	5.28	4.67	2.13

Table 3: Statistics of gap to diameter ratio (G/D) variation for 70 species with body lengths.

5.2.2. Force generation

We processed data from strain gauge measurements and obtained lift coefficient (C_L) and drag coefficient (C_D) as described in the methods chapter. Both coefficients were obtained after averaging forces for 30 cycles during both clap and fling phases. Figure *27* shows time variation of C_L and C_D during both clap and fling phases for all the wing models at Re_c = 10. We observed that the force coefficients (C_L, C_D) followed the same trend across all wing models of varying G/D during both clap and fling. The maximum value of force coefficients ($C_{L,max}$, $C_{D,max}$) decreased with increasing G/D during both clap and fling (Figure *28*).

Fling phase

From the time variation of drag coefficient for bristled wing models *(Figure 27A)*, we observed drag force peaked close to 50% of the fling time and then remained nearly constant for the rest of the fling duration. In contrast, we observed the generation of negative drag force just after the peak value the solid wing model. This negative drag force value was observed to decrease with increase in G/D. As suggested in the previous study, the negative drag force generation could be related to the start of translational motion at 50% of fling time (*Figure 9*). The negative drag force was observed to be negligible for all the bristled wing models. This could be due to fact that the bristled wings allow the flow to leak between the bristles, dampening fluctuations in drag force variation. While the drag force was observed to follow the same trend for all bristled wing models, it was also observed that the drag force (C_D) was decreasing with increasing G/D. This supports the argument that bristles reduce the forces to fling the wings.

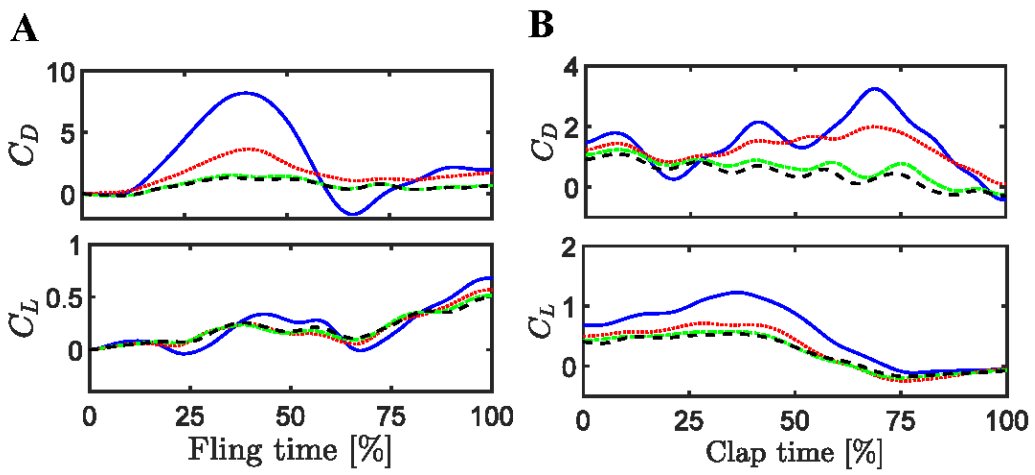

Figure 27: Variation of force coefficients as a function of cycle time for solid wing (——), G/D = 5 (·····), 11 (— · —), 17 (– – –) (A), (B) Drag coefficient (C_D) (top) and lift coefficient (C_L) (bottom) at Re_c = 10 calculated from filtering the strain gauge data during fling, clap respectively.

While the drag force (C_D) was found to decrease substantially with increasing G/D, the lift force (C_L) looked to be invariant with increasing G/D at Re_c = 10. If we look at the plot for C_L during the fling for any wing model, we can observe lift force to fluctuate largely throughout entire fling duration. Also, all the wings models are observed to follow the same trend through entire fling duration.

Clap phase

From the plot (Figure *27B*) for coefficient of drag (C_D) versus clap time we observed drag force (C_D) to fluctuate largely during entire clap duration for all the wing models at Re_c = 10. However, all the wing models were observed to follow the same trend during the complete clap duration. As mentioned earlier, these fluctuations could be due to combination of translation and rotational motion of the wing during the clap phase. From the kinematics *Figure 9*, we can see that the wing translates in addition to the rotation motion during entire clap phase which supports the idea that translational motion bring in some uncertainty in the forces. Also these fluctuations looks to settle with increase in G/D at same Re_c. Hence, this finding supports our statement from the previous study that bristled wings allow the flow to leak between the bristles causing the forces to stabilize during clap motion. In addition, the drag forces in the form of C_D was found to decrease slightly with increasing G/D at Re_c = 10.

The plots for C_L versus clap time shows the lift force in terms of C_L was found to increase for about 50% of the clap time and then start to decrease for remaining time at Re_c = 10. This trend was observed to be consistent with all the wing models. However, the lift force (C_L) was found to decrease slightly with increasing G/D at Re_c = 10.

Peak lift and drag force analysis during both clap and fling

Figure 28 (A, B) shows maximum drag coefficient ($C_{D,\max}$) , maximum lift coefficient ($C_{L,\max}$) and maximum lift coefficient over maximum drag coefficient ($C_{L,\max}$ / $C_{D,\max}$) plotted versus G/D

ratio during both clap and fling phase at Re_c = 10. With increasing G/D, $C_{D,\max}$ was decreasing while $C_{L,max}$ was found to have little effect compared to $C_{D,max}$ during both clap and fling times. Hence, maximum lift coefficient over maximum drag coefficient ($C_{L,max}$ / $C_{D,max}$) would increase with increase in G/D during both clap and fling times. This theory is in accordance with the plot $C_{L,max}$ / $C_{D,max}$ versus G/D shown in the *Figure 28* during both clap and fling times.

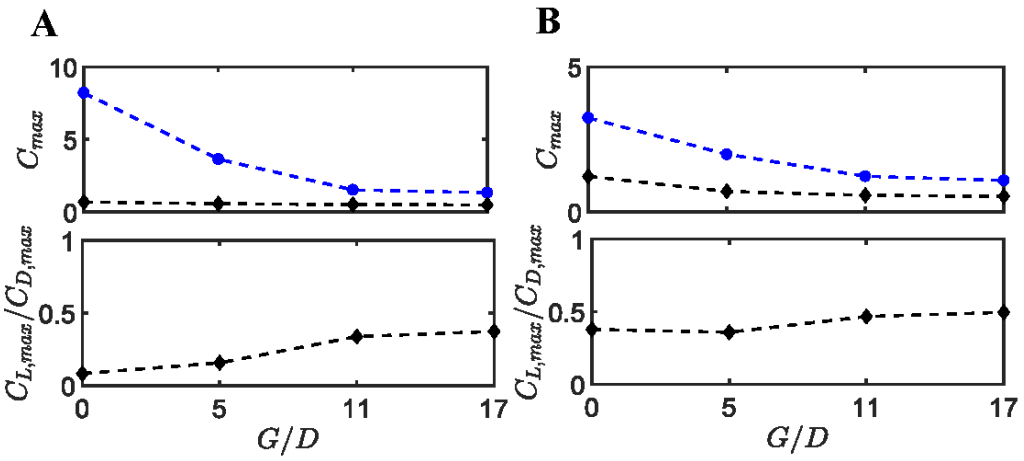

Figure 28: Variation of peak force coefficients, $C_{D,\max}$ (--●--), $C_{L,\max}$ (--◆--) and ratio of peak lift coefficient to peak drag coefficient with G/D, (A) Fling, (B) Clap

5.2.3. Leakiness

In order to quantify our forces with flow structures, we looked at how leakiness between the bristles was affecting the force generation. After post-processing the spanwise PIV data for all the wing models at Re_c = 10, Leakiness (*Le*) was calculated with the help of customized MATLAB script file using the equations (9),(10), (11),(12). *Figure 29A,Figure 31A* shows the plots for Leakiness (*Le*) versus fling time and clap time for all the wing models at Re_c = 10. From the plots, we can observe that leakiness follows the same trend for all bristled wing models.

Fling

From the plot for *Le* versus fling time, *Le* was observe to vary largely during complete fling duration. In addition, *Le* was observed to increase with increasing G/D ratio at Rec = 10 at all the time points tested. However, it was also observed that *Le* was approaching close to value 1 at

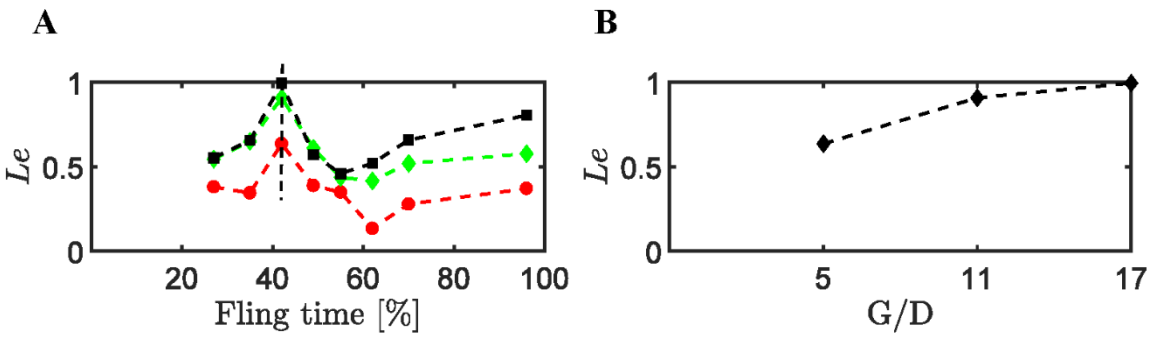

Figure 29: Leakiness (*Le*) as a function of fling time and G/D ratio, G/D = 5(-●-), 11(-■-), 17(-◆-), (A) (left) Leakiness was observed to peak at ~40% of fling time (37.5% fling angle) for all the bristled wing models, B) (right) Leakiness vs G/D at ~40% fling time (dashed line in part A).

37.5% fling angle (≈ 40% of fling time) for all the wing models. To verify how *Le* behaves at that particular time point for all the wing models, we looked at leakiness (*Le*) versus G/D ratio at 37.5% fling angle (≈ 40% of fling time). From the *Figure 29(A)*, we observed that at the time point (≈ 40% of fling time), *Le* increases with increase in G/D ratio and reaches the maximum value 1.

As mentioned in the previous study, In order to generate a better understanding of how the flow structures look like along the spanwise direction during the fling time, we plotted vector fields using the post-processed data from spanwise PIV into tecplot (*Figure 30A*). From the plots, we observed the formation of small recirculating vortices around the bristles and these vortices looked to increase with increasing fling time until about 40% of fling duration as shown in the

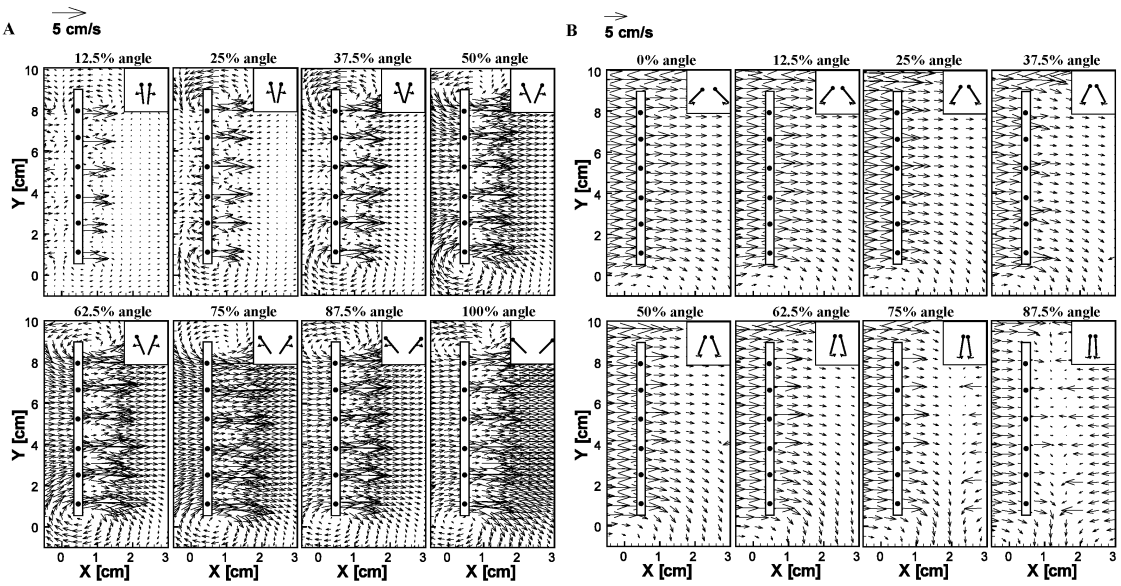

Figure 30: Velocity vector fields describing the flow through the bristles during (A) fling (left) and (B) clap (right) for a bristled wing model (G/D=11) at Re_c=10. In the case of fling, recirculating vortices form in between the bristles at 37.5% of fling angle and eventually dissipate at higher angles. However, recirculating vortices in between the bristles are not observed in clap.

Figure *30*A. However, note that we did not find any recirculating vortices for bristled wing model with G/D = 5. The plots for this wing model can be found in the appendix section. This could be justified by the fact that the bristled wing model with G/D = 5 have lesser gap between the bristles causing the recirculating vortices around each bristle to diminish. Hence, *Le* values were

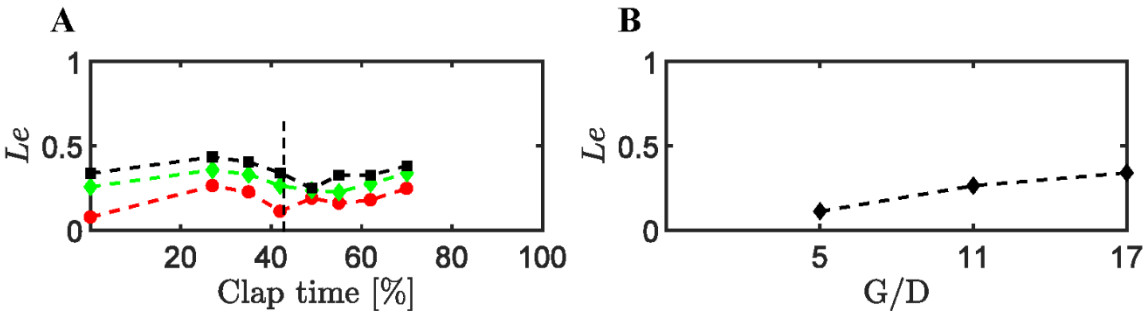

Figure 31: Leakiness (*Le*) as a function of clap time and G/D ratio, G/D = 5(-●-), 11(-■-), 17(-◆-), (A) (left) Leakiness was observed to have little effect with change in G/D ratio during clap phase, B) (right) Leakiness vs G/D at ~40% fling time (dashed line in part A).

observed to be lower for bristled wing model with G/D = 5. This could support our statement from the previous study that recirculating vortices are playing a major role in enhancing the leakiness for bristled wing models.

Clap

As in fling, *Le* was also varying largely during clap. However, from the plots (*Figure 31A*), *Le* values were observed to be lower during clap compared to that of fling for all the bristled wing models at Re_c = 10. It was also observed that *Le* was increasing with increasing G/D at all the time points. The plot showing *Le* versus G/D at 37.5% fling angle (≈ 40% of fling time) supports the above statement. To investigate why leakiness values during clap were reduced, we looked at the vector plots along spanwise direction during clap time. As specified in the previous study, even in the present study we did not observe the formation of any recirculating vortices for all the bristled wing models during clap (*Figure 30B*), which could be the reason for drop in *Le* values.

5.2.4 Circulation

Figure 32, Figure 33 shows the processed plots with velocity vector fields and vorticity contours at Re_c = 10 for the wing models G/D = 5,11 at 8 different time points in a cycle (25%, 50%, 75%, 100% of fling angle, 0%, 25%, 50%, 75% of clap angle). For the vorticity plots of solid and G/D =17 wing models please refer the *Figure 23, Figure 24* respectively. For each of these plots during clap and fling, PIV data was collected at the plane HP as referred in the *Figure 13*(B). From the plots, with increasing fling angle, we observe the formation of stronger leading edge vortex compared to trailing edge vortex at all time points for all the wing models. While during clap, we observe the formation of stronger trailing edge vortex compared to leading edge vortex for all the wing models at all time points. Comparing the vortices for the all the wing models, as specified in the previous study we observed that both the leading and trailing edge vortices are weaker for bristled wing models compared to solid wing during both clap and fling times. While

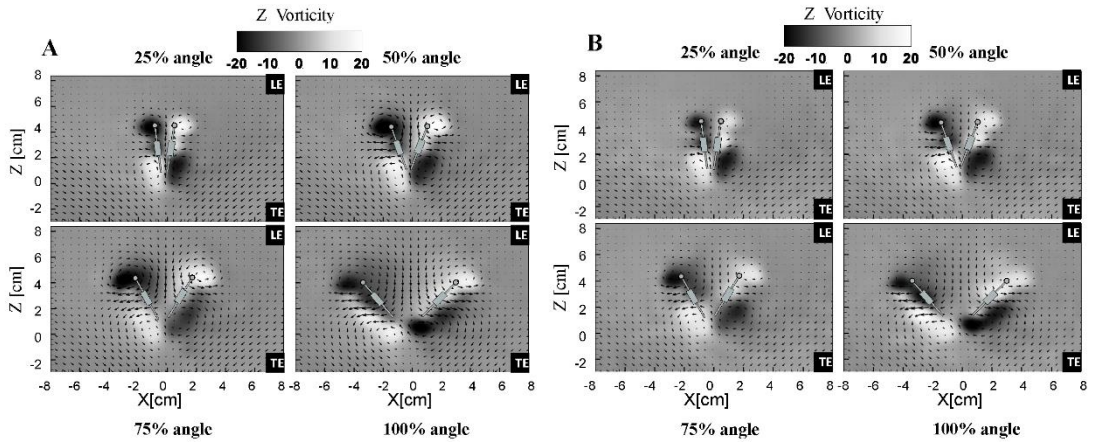

Figure 32: Vector and vorticity plots for bristled wing models of G/D = 5, 11 during fling. A) Bristled wing model of G/D =5 at 25%, 50%, 75%, 100% fling angle, B) Bristled wing model of G/D =11 at 25%, 50%, 75%, 100% fling angle, LE - leading edge, TE - Trailing edge.

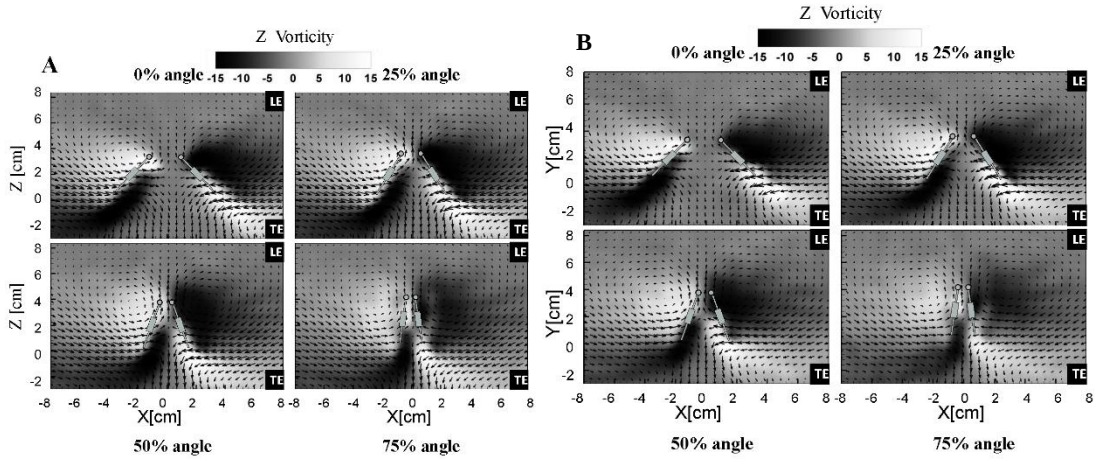

Figure 33: Vector and vorticity plots for bristled wing models of G/D = 5, 11 during clap. A) Bristled wing model of G/D =5 at 0%, 25%, 50%, 75% clap angle, B) Bristled wing model of G/D =11 at 0%, 25%, 50%, 75% clap angle, LE - leading edge, TE - Trailing edge.

for bristled wing models, with increase in G/D we observe decrease in strength of leading and trailing edge vortex. In addition, from the plots we can observe the velocity vectors were decreasing with increasing in G/D at Re_c =10 during both clap and fling times. Since the forces generated by the wings are comparable to circulation at leading edge and trailing edge, we calculated circulation at the Leading edge Γ_{LEV}, at the Trailing edge Γ_{LEV} using the equations (13),(14), (15) with the help of customized MATLAB script file and plotted as shown in *Figure*

34. Circulation plots at Re_c = 10 during clap and fling times were presented in the *Figure 34* (A, B) respectively. From the plot for leading edge vortex circulation (Γ_{LEV}) versus fling time, we observe that Γ_{LEV} was decreasing with increasing in G/D.

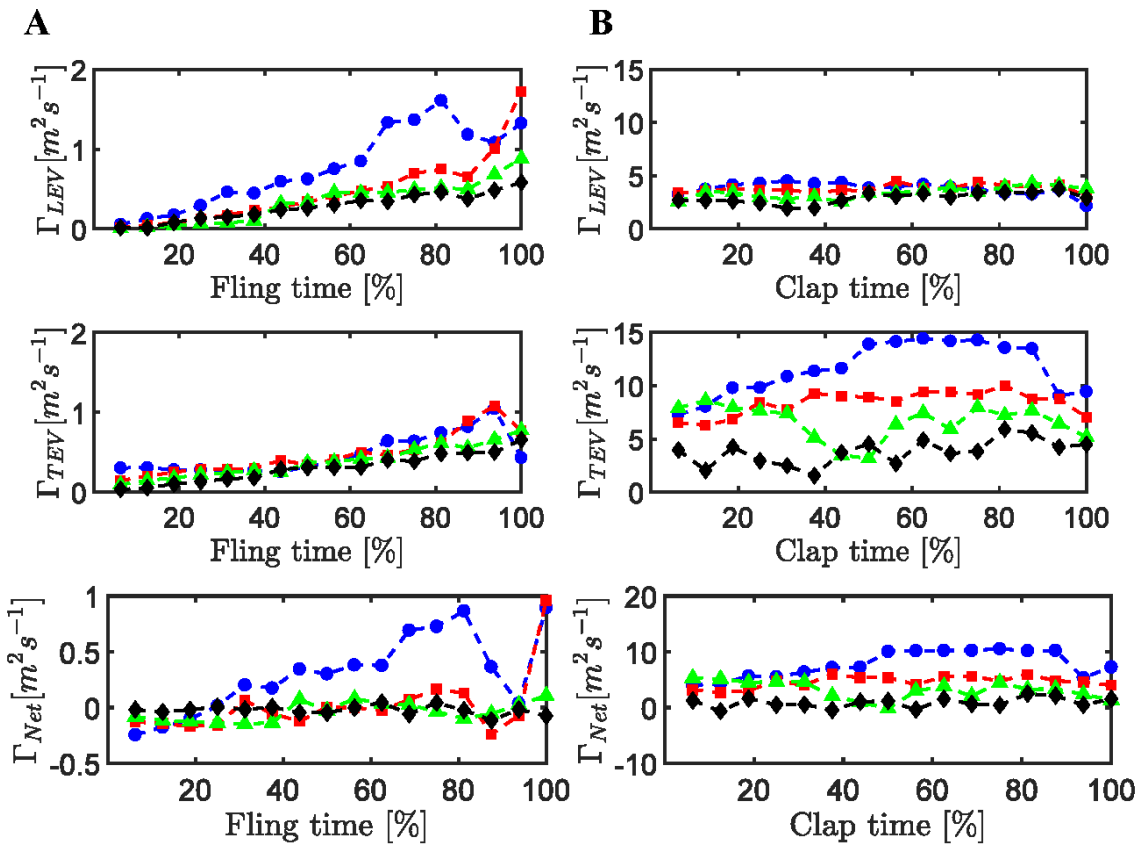

Figure 34: Solid(-●-), G/D = 5(-■-), 11(-▲-), 17(-◆-), Circulation in fling (A) and clap (B) at Re_c = *10*. Top: LEV circulation Γ_{LEV}, middle: TEV circulation Γ_{TEV}, and bottom: net circulation Γ_{Net} .

While the drop in Γ_{LEV} was larger from solid to bristled wing model, Γ_{LEV} was observed to be in close range for all the bristled wing models (G/D =5, 11, 17). However, from the plots for Γ_{TEV} versus fling time, Γ_{TEV} does not look to change with increase in G/D ratio. For any bristled wing model (G/D =5, 11, 17) we don't see much change in Γ_{LEV}, Γ_{TEV} throughout the entire fling at Re_c = 10. Therefore net circulation (Γ_{Net}), which is defined as the Γ_{Net}=||Γ_{LEV}| - |Γ_{TEV}|| was observed

to decrease from solid to any bristled wing model. While Γ_{Net} for all bristled wing model (G/D =5, 11, 17) was found to fall in the same range.

From the plot for leading edge vortex circulation (Γ_{LEV}) versus clap time, we observe that Γ_{LEV} does not look to change with increase in G/D ratio. However, from the plots for Γ_{TEV} versus clap time, Γ_{TEV} was decreasing with increasing in G/D. For any bristled wing model (G/D =5, 11, 17) we don't see much change in Γ_{LEV} throughout the entire clap at Re_c = 10 while Γ_{TEV} was observed to decrease with increase in G/D. Therefore net circulation (Γ_{Net}), which is defined as the Γ_{Net}=||Γ_{LEV}| - |Γ_{TEV}|| was observed to decrease from solid to any bristled wing model. Also, Γ_{Net} for bristled wing models (G/D =5, 11, 17) was found to to decrease with increase in G/D ratio.

5.3. Discussion

In this study, we found that (1) G/D ratio of the forewing in the order of Thysanoptera fall in the range of 2-12 and the mean G/D was found to be 5. (2) During wing-wing interactions, aerodynamic forces (C_L, C_D) decreases with increase in G/D ratio. (3) Although the peak drag force was reduced with increase in G/D ratio, the decrease was found to be much significant between solid and bristled wing model (G/D = 5, 11, 17). This suggests that leaky flow helps in reducing the drag force. (4) The drop in peak lift force C_L was not large with increase in G/D during both clap and fling phases. This shows that increase in G/D ratio have little effect on lift force generation in comparison to drag force. (5) The peak lift over drag ratio ($C_{L,\max}$ /$C_{D,\max}$) was increasing with increase in G/D ratio during both clap and fling times. However, the increase in peak ratio was much significant between solid, bristled wing model compared to its increase among bristled wing models. (6) Even leakiness and circulation were varying significantly between solid, bristled wing model in comparison to its variation among bristled wing models. From the above findings, we propose that bristled wings provides aerodynamic benefits over solid

wings during flapping flight. However increasing the G/D ratio for a bristled wing model does not show much improvement in aerodynamic performance.

A previous study on bristled wings suggests that with increasing G/D, although the lift force was reduced, there was substantial decrease in peak drag force [17] which is in support with our findings. Another previous work suggests that for a bristled wing model, fluid dynamic forces gets reduced [9].Our results shows that although the lift and drag forces decreased with increase in G/D, the peak lift over drag ratio appeared to have a very little effect.

From our results, we noticed that during both clap and fling times, with increase in G/D ratio, both C_L and C_D were decreased. However, the peak lift over drag ratio ($C_{L,\,\max}$ / $C_{D,\,\max}$) was found to increase a little with increase in G/D ratio. This has raised many question such as 1) Does leaky flow had a role in increasing aerodynamic performance? 2) Since the conventional lift generation was based on circulation, how does circulation help in quantifying the lift force with increasing G/D ratio during wing-wing interaction? To have a better understanding on these questions, let us look into the results for leakiness and circulation during both clap and fling times.

From the leakiness results, we suggested that *Le* was increasing with increase in G/D ratio during both clap and fling. While from the force results, the peak drag force was reduced with increasing G/D. Peak lift force had very little effect with increase in G/D ratio. This suggests that leakiness have larger effect on drag force in comparison to lift force during flapping flight. Hence, from this and using our results we can draw to a conclusion that increase in leakiness decreases the drag force. To verify how the leakiness could affect drag reduction, we looked at the flow structures for all the wing models during entire clap and fling times separately. During fling, with increasing time we observed the formation of little recirculating vortices around each bristle. The strength of these recirculating vortices was observed to increase with increase in G/D ratio. These

vortices looked to dissipate at about 50% of fling time for all G/D. Note that during fling, translational motion starts at 50% of fling time and this could be one of the reasons for dissipation of these vortices. However, from the flow structures plots during clap we do not see the formation of any recirculating vortices around the bristles. While from the force plots during fling, we see large reduction in drag force with increase in G/D. However, during clap we do not see drag reduction at such a large scale. These results could be justified by suggesting that during fling, formation of recirculating vortices helped in increasing the flow leakage between the bristles, which in turn helped in decreasing the drag force at larger scale.

From the conventional aerodynamics point of view, circulation at the leading edge (LE) and trailing edge (TE) are the source for the generation of lift force. From the circulation plots, during fling phase we can observe that the net circulation Γ_{Net} had a very little effect with increase in G/D. From Wu 1981 [46] paper, net circulation is directly proportional to the lift force generation (Lift (L) $\propto \Gamma_{Net}$). Hence, lift force does not change much with increasing G/D ratio. This was evident in the force plots for C_L during entire fling. However, during clap the net circulation Γ_{Net} was found to decrease with increase in G/D ratio in comparison to fling. Hence, lift force decreases with increase in G/D ratio. This was also in support with the force plots for C_L during clap time.

Therefore, altogether these results supports our proposal that bristled wings provides aerodynamic benefits over solid wings during flapping flight. However, bristled wing model does not show much improvement in aerodynamic performance after G/D ratio of 11.

CHAPTER VI

CONCLUSIONS

6.1. Overview

Insect flight has been a controversial study for a long period. Due to the large range of body lengths of flying insects (5 - 250 mm), we can expect that a single theory may not be applicable across all flight-capable insects. Previous studies have shown that the aerodynamics and kinematics of larger insects are different from the smaller insects ([8], [32], [47]). Tiny insects such as fairy flies, thrips and parasitoid wasps have body lengths less than 5 mm and their wingspan is as low as 0.5 mm. Most of the tiny insects are reported to fly at a Reynolds number (defined as ratio of inertial to viscous forces) on the order of 10. At these low Reynolds numbers, viscous forces are dominant. Thus, flapping in these small size scales is expected to be energetically demanding as resistive forces on their wings increases. Nevertheless, field observations of thrips ([8], [14], [15], [37]) show that these insects can still manage to generate sufficient lift force to support their body weight. In contrast to larger insects, freely-flying thrips have been observed to use wing-wing interaction via the Weis-Fogh [27] 'clap and fling' mechanism [24] as a part of their wing kinematics. In addition, the wings of many tiny insects show the presence of bristles or hair-like structures attached to a solid membrane [39], [48]–[51]. The broad motivation of this study was to examine whether bristled wings can provide aerodynamic benefits in the flapping flight of tiny insects. There is a notable paucity of free-flight recordings of tiny insects in published literature. This is primarily owing to technological

challenges associated with imaging length scales on the order of 100 microns while simultaneously resolving time scales on the order of 100 Hz. Further, experimental studies at the organismal level are also challenged by the inability to control the animal position and orientation. To address these challenges, we designed and developed a dynamically scaled robotic model that can mimic the clap and fling wing-wing interaction. The wing motion was driven by stepper motors that were programmed to execute clap and fling kinematics as described in a previous study [40]. Scaled-up physical models of bristled wings were tested in this facility in comparison to solid wings of equivalent cross-section and thickness. Time-varying forces were obtained using strain gauges bonded to the root of the wing models. Particle image velocimetry (PIV) measurements were acquired to visualize the chordwise flow structures and spanwise flow through the bristles. Our results show that for Reynolds number in the range of 5-15, bristled wings decrease the drag force required for clap and fling and augment the peak lift to peak drag ratio as compared to solid wings.

The subsequent sections of this chapter highlight the findings from the two specific aims that were conducted as a part of this work: 1) Use a dynamically scaled robotic clap and fling simulator to quantify the aerodynamic forces and flow structures for solid and bristled wing physical models under varying *Re* from 5-15, 2) (a) Conduct morphometric analysis of published data of bristled wings in the order Thysanoptera and quantify the biological variability in G/D ratio, (b) Design bristled wing models with biologically relevant G/D and quantify the aerodynamic forces and flow structures generated by these wing models at *Re*=10.

6.2. Effect of varying Reynolds number

For the first specific aim, we developed a dynamically scaled robotic model that can mimic the clap and fling kinematics as described in Miller and Peskin [40]. Aerodynamic forces and flow structures were comparatively examined in physical models of 1 solid wing pair (G/D=0) and 1

bristled wing pair (G/D =17) for chord-based Reynolds number (Re_c) varying from 5-15. Each wing pair was driven using stepper motors in the robotic setup, programmed to perform clap and fling kinematics[40]. Strain gauges were used to determine lift and drag coefficients, while PIV was used to: (a) quantify the circulation (or strength) of the leading edge vortex (LEV) and the trailing edge vortex (TEV), and (b) quantify the flow leaking through the bristles along the wing span via a non-dimensional quantity (leakiness). Our results showed that: 1) for any particular Re_c in the range of 5-15, peak lift to peak drag ratio was larger for the bristled wing model as compared to the solid wing model in both clap and fling phases; and 2) peak lift over peak drag ratio was generally invariant with increasing Re_c for solid and bristled wings during both clap and fling phases. In general, for any particular Re_c, aerodynamic force coefficients (C_L, C_D) were lower for bristled wings as compared to solid wings during both clap and fling phases. However, the reduction in drag coefficient (C_D) for bristled wing (compared to solid wing) was notably larger than the decrease in lift coefficient (C_L) for bristled wing (compared to solid wing) during clap and fling phases. Thus, the drag force required to clap and fling a wing pair was significantly lower for bristled wings as compared to solid wings. Due to this disproportionally larger reduction of drag in bristled wings (as opposed to lift), peak lift over peak drag ratio ($C_{L,max}$ /$C_{D,max}$) was effectively increased for bristled wings when compared to solid wings at identical Re_c. These observations suggest that bristles likely play a uniquely important role during flapping flight of tiny insects via: 1) lowering force needed to fling the wings apart or clap the wings together; 2) augmenting aerodynamic efficiency (defined as the ratio of lift to drag forces); and 3) maintaining nearly constant aerodynamic efficiency across two orders of variation in Re_c (e.g., due to change in wing length and/or wingbeat frequency).

To examine the fluid dynamic mechanism underlying the large drag reduction in bristled wings, phase-locked PIV data was acquired along the span of the bristled wing model and determine leakiness of flow through the bristles. Leakiness is a non-dimensional quantity that has been used

in previous studies of bristled appendages [[10], [42]] to quantify the proportion of volumetric flow rate that is leaked through the appendages in the direction opposite to the bulk flow pattern (latter being direction of wing motion for this study). Leakiness was found to vary significantly during the entire fling phase and reach the maximum possible value of 1 for $Re_c > 8$ at roughly 40% of the fling cycle. An observation of the spanwise flow field at this cycle time point (corresponding to maximum leakiness) showed the formation of small-scale vortices around the bristles. These small-scale vortices recirculated the entire volumetric flow passing through the bristles in the direction opposite to the wing motion. The additive volume of fluid that is fluxed into the space between two bristled wings in fling (whenever leakiness is non-zero) is expected to increase the pressure in this domain and thus reduces the force required to fling the wings apart Figure *35*.

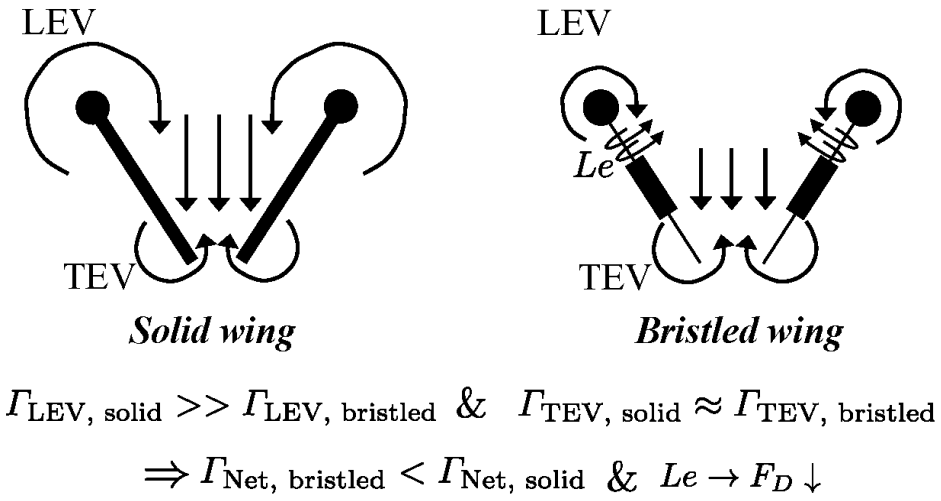

Figure 35: Cartoon showing the differences in flow structures between solid and bristled wings during fling phase. LEV=leading edge vortex; TEV=trailing edge vortex; *Le* = leakiness; Γ = circulation of LEV or TEV; net circulation $\Gamma_{\text{Net}} = |\Gamma_{\text{LEV}}| - |\Gamma_{\text{TEV}}|$

Interestingly, we did not observe the formation of these small-scale vortices around the bristles during clap phase, where drag reduction by bristled wing model was lower than drag reduction in

fling (drag reduction of bristled wing being compared to solid wing in each phase). This suggests that the small-scale recirculation around the bristles plays a crucial role in determining the extent of drag reduction achievable by interacting bristle wings. While previous computational studies [8], [10] have shown drag reduction to be a primary consequence of bristled wing-bristled wing interaction, they did not observe these small-scale vortices and thus were unable to clarify the physical mechanism behind the observed drag reduction (other than conjecturing that flow must be leaked through the bristles). It is important to note that the existence of the small-scale vortices around the bristles is not a requirement for non-zero leakiness (e.g., leakiness >0 in clap phase, despite no vortices observed around bristles), but rather for maximizing the proportion of reverse flow that is displaced between the bristles.

We sought to address a second limitation of previous computational studies of wing-wing interaction with bristled wings [8], [10], where chordwise flow structures (LEV and TEV) were not examined and interpreted in the context of how they impact the lift force generated in clap and fling. Starting from chordwise PIV data, we computed the circulation (strength) of the LEV and TEV for both the solid and bristled wing pairs in clap and fling phases. Irrespective of Re_c, we observed the following in fling: 1) circulation of LEV is larger for solid wings as compared to bristled wings; and 2) TEV circulation is nearly unchanged when comparing solid and bristled wings (Figure *35*). We observed the exact opposite trends for LEV-TEV circulation in clap phase (for any particular Re_c): 1) circulation of TEV is larger for solid wings as compared to bristled wings; and 2) LEV circulation is nearly unchanged when comparing solid and bristled wings. These findings suggest that leakiness effectively diminishes the vorticity of LEV (fling) or TEV (clap), while minimally impacting the vorticity in the region proximal to point of rotation (trailing edge in fling, leading edge in clap). The geometric positions of the wings performing clap and fling leads to asymmetries in LEV and TEV based on point of wing rotation. Leakiness serves to

diminish vortex strength (in both LEV and TEV), ostensibly via increasing pressure within the cavity formed by the interacting wing pair.

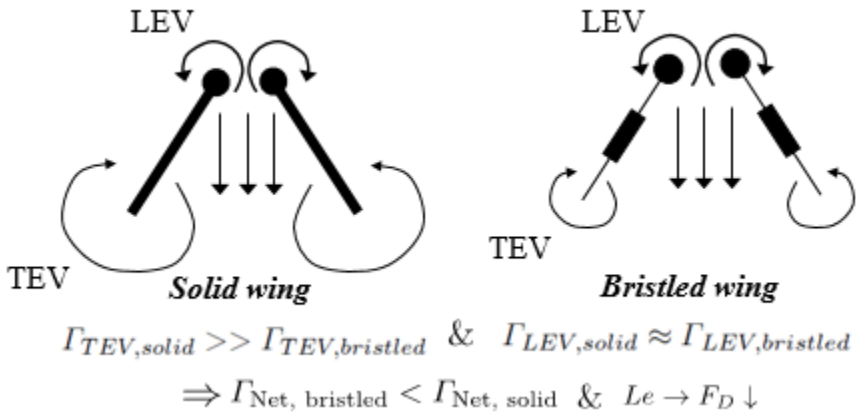

Figure 36: Cartoon showing the differences in flow structures between solid and bristled wings during clap phase. LEV=leading edge vortex; TEV=trailing edge vortex; *Le* = leakiness; Γ = circulation of LEV or TEV; net circulation $\Gamma_{\text{Net}} = |\Gamma_{\text{LEV}}| - |\Gamma_{\text{TEV}}|$

In terms of lift reduction by bristled wings, we determined net circulation in both clap and fling as the difference between absolute value of LEV circulation and absolute value of TEV circulation. Based on Wu's theory[46] and its interpretation offered by Miller and Peskin (2004) [32], the net circulation over the wing can be stated to be proportional to the lift. Regardless of Re_c, we observed that net circulation was lower for bristled wings as compared to solid wings. This suggests that lift reduction in bristled wings was a consequence of reduction in net circulation (Fig. 35 and 36).

6.3. Effect of varying ratio of bristle spacing to bristle diameter (G/D)

For the second specific aim, we analyzed published forewing images in 70 species of thrips to quantify ratio of the spacing (or gap G) between a pair of bristles to the bristle diameter (D). Both these lengths were measured all along the wing surface area and average G/D was calculated for every species that was analyzed. Based on the biologically observed variation of G/D in thrips (2

to 12), physical models of two bristled wing pairs were fabricated (G/D=5 and 11) and tested using the robotic clap and fling facility.

The results of force measurements showed that during wing-wing interactions, both aerodynamic force components (represented via dimensionless coefficients of lift (C_L) and drag (C_D)) decreased with increasing G/D. Although the peak drag force was reduced with increase in G/D ratio, significant drag reduction was observed when comparing any of the tested bristled wing models against the solid wing model. This suggests that the primary aerodynamic consequence of leaky flow through bristles is in reducing the drag force during clap as well as in fling. In contrast, the drop in peak lift force ($C_{L,max}$) with increasing G/D was not as large during both clap and fling phases. This suggests that increase in G/D has a minor impact on lift reduction with bristled wings when compared to solid wings. In terms of peak aerodynamic efficiency, the peak lift to peak drag ratio ($C_{L,max}$ /$C_{D,max}$) increased with increasing G/D during both clap and fling phases. However, the increase in peak lift to peak drag ratio was more pronounced when comparing solid and any of the tested bristled wing models. The net circulation varied significantly when comparing the solid wing and any of the bristled wing models, and only showed small variation among bristled wing models of varying G/D. From the above findings, we propose that bristled wings provide aerodynamic benefits over solid wings during flapping flight. However, the aerodynamic efficiency reaches a constant value after G/D ratio of 11.

Overall, the results of both specific aims show that bristled wings indeed provide aerodynamic benefits over solid wings performing clap and fling within a low Reynolds number range (Re_c~O(10)) that is biologically relevant to tiny insect flight. The aerodynamics benefits obtained via use of bristled wings when compared to solid wings include: 1) drag reduction; and 2) augmentation of lift to drag ratio, typically viewed as a metric of aerodynamic efficiency. In addition, aerodynamic efficiency (C_L/ C_D) does not notably vary within the range of Re_c tested (5-15). There was a clear increase in aerodynamic efficiency when comparing bristled wings to solid

wings at any Re_c or G/D. Finally, increasing G/D ratio of bristled wings after a value of 11 did not provide an increase in aerodynamic efficiency. Interestingly, our forewing image analyses in 70 species of thrips showed G/D varied between 2 and 12. The benefit realized when increasing the bristle spacing (increased lift over drag ratio) is also accompanied with a tradeoff---the lift generated decreases with increasing G/D. Thus, if we were to assume that the sole purpose of lift is for weight support, the inter-bristle spacing (G) is a crucial design variable that can determine the maximum lift that can be generated as well as the aerodynamic efficiency augmentation achievable using bristled wings.

In addition to aerodynamic efficiency, bristles may have other benefits that were not considered in this study. For instance, the inclusion of bristles may reduce wing weight and thus reduce the demand for lift generated. Reduction of forces needed to clap and fling a pair of wings at low Reynolds number can reduce the muscular energetic workload necessary for a wingbeat. Wing bristles have been shown to assist in folding and unfolding the wing[28]. Finally, previous studies have suggested that bristles may enhance electrostatic charges to help in dispersal [10], [52], or act as airflow and vibration sensors [53], [54].

6.4. Limitations

It is important to note some of the assumptions that were made in this study, including: 1) minimal flow along the spanwise direction of the wing (which is to be expected due to low *Re*); 2) wall effects from aquarium walls were negligible; and 3) flow around each of the wings in an wing pair undergoing clap and fling are symmetrical, as the prescribed motion kinematics for each wing in a wing pair was symmetrical.

While our study only considered clap and fling phases and excluded the other aspects of wingbeat kinematics that includes flapping translation and wing rotation, previous studies [29], [40] have shown that both lift and drag peaks occur during clap and fling. Another limitation of this study is

the design of wing models that were rectangular in cross-section, with bristles only attached laterally and symmetric about either side of the centerline (long-axis) of a solid membrane. However, forewings of tiny insects are usually teardrop-shaped, and bristles are attached to solid membrane both laterally at the sides and longitudinally at wing tip. Further, the forewing bristles in tiny insects need not always be symmetric about the centerline of the solid membrane. These factors will need to be accounted for in future studies.

In addition to the shape, the wings of tiny insects are flexible. We can expect that there would be non-uniform flow along the wing span, due to wing pair performing a 'peel' as opposed to fling, which in turn would impact the leakiness as well as net circulation around the wings. Flexibility was not considered in this study and will need to be accounted for in future studies.

6.5. Recommendations for future work

The findings of this study on bristled wings raises numerous questions related to flapping flight kinematics in tiny insect flight and the specific role of bristles. A previous computational study by Miller and Peskin [29] showed that wing flexibility can reduce drag forces required to fling the wings apart during wing-wing interactions. Images of freely-flying thrips [8] show that the solid membrane portion of thrips wings is flexible. Thus, studying the coupled effect of bristled wings with flexibility would provide a more realistic representation of the wings, and evaluate whether flexibility and leakiness work additively in further decreasing drag during fling as compared to this study, or which among the two mechanical design variables are of higher order importance in enhancing aerodynamic efficiency. In addition, a recent study[55] has shown that due to wing-body interaction, there was 18.7% increase in total lift production for a wing-body model in comparison to only wing model. Thus wing-body interaction could play a major role in lift enhancement, and this needs to be studied further.

REFERENCES

[1] J. Huber and J. Noyes, "A new genus and species of fairyfly, Tinkerbella nana (Hymenoptera, Mymaridae), with comments on its sister genus Kikiki, and discussion on small size limits in arthropods," *J. Hymenopt. Res.*, vol. 44, pp. 17–44, 2013.

[2] A. P. Willmott, C. P. Ellington, and A. L. R. Thomas, "Flow visualization and unsteady aerodynamics in the flight of the hawkmoth, *Manduca sexta*," *Philos. Trans. R. Soc. B Biol. Sci.*, vol. 352, no. 1351, pp. 303–316, 1997.

[3] G. R. Spedding and T. Maxworthy, "The generation of circulation and lift in a rigid two-dimensional fling," *J. Fluid Mech.*, vol. 165, no. 1, p. 247, 1986.

[4] C. P. Ellington, "The Aerodynamics of Hovering Insect Flight . IV . Aerodynamic Mechanisms," vol. 305, no. 1122, pp. 79–113, 1984.

[5] M. H. Dickinson, F. O. Lehmann, and S. P. Sane, "Wing Rotation and the aerodynamics basis of insect flight," *Science.*, vol. 284, no. 1999, pp. 1954–1960, 1999.

[6] J. M. Birch, W. B. Dickson, and M. H. Dickinson, "Force production and flow structure of the leading edge vortex on flapping wings at high and low Reynolds numbers," *J. Exp. Biol.*, vol. 207, no. 7, pp. 1063–1072, 2004.

[7] C. P. Ellington, C. van den Berg, A. P.Willmont, and A. L. R. Thomas, "Leading edge vortices in insect flight," *Nature*, vol. 348, pp. 626–630, 1996.

[8] A. Santhanakrishnan, A. K. Robinson, S. Jones, A. A. Low, S. Gadi, T. L. Hedrick and

L. A. Miller, “Clap and fling mechanism with interacting porous wings in tiny insect flight,” *J. Exp. Biol.*, vol. 217, no. 21, pp. 3898–3909, 2014.

[9] S. Sunada, H. Takashima, T. Hattori, K. Yasuda, and K. Kawachi, “Fluid-dynamic characteristics of a bristled wing,” *J. Exp. Biol.*, vol. 205, pp. 2737–2744, 2002.

[10] S. K. Jones, Y. J. J. Yun, T. L. Hedrick, B. E. Griffith, and L. A. Miller, “Bristles reduce the force required to ‘fling’ wings apart in the smallest insects,” *J. Exp. Biol.*, vol. 219, no. 23, pp. 3759–3772, 2016.

[11] P. Trizila, K. C-K, H. Anono, S. W, and M. Visbal, “Low-Reynolds-Number Aerodynamics of a Flapping Rigid Flat Plate,” *AIAA J.*, vol. 49, no. 4, pp. 806–823, 2011.

[12] M. Percin, Y. Hu, B. W. van Oudheusden, B. Remes, and F. Scarano, “Wing Flexibility Effects in Clap-and-Fling,” *Int. J. Micro Air Veh.*, vol. 3, no. 4, pp. 217–228, 2012.

[13] I. Terry, “Thrips and weevils as dual, specialist pollinators of the Australian cycad Macrozamia communis (Zamiaceae),” *Int. J. Plant Sci.*, vol. 162, no. 6, pp. 1293–1305, 2001.

[14] D. G. Riley, S. V. Joseph, R. Srinivasan, and S. Diffie, “Thrips Vectors of Tospoviruses,” *J. Integr. Pest Manag.*, vol. 1, no. 2, pp. 1–10, 2011.

[15] D. R. Jones, “Plant viruses transmitted by thrips,” *Eur. J. Plant Pathol.*, vol. 113, no. 2, pp. 119–157, 2005.

[16] B. J. Crespi, D. A. Carmean, and T. W. Chapman, “Ecology and evolution of galling thrips and their allies,” *Annu. Rev. Entomol*, vol. 42, pp. 51–71, 1997.

[17] S. K. Jones, R. Laurenza, T. L. Hedrick, B. E. Griffith, and L. A. Miller, “Lift vs. drag based mechanisms for vertical force production in the smallest flying insects,” *J. Theor. Biol.*, vol. 384, pp. 105–120, 2015.

[18] J. M. Birch and M. H. Dickinson, “Spanwise flow and the attachment of the leading-edge vortex on insect wings.,” *Nature*, vol. 412, no. 6848, pp. 729–733, 2001.

[19] S. P. Sane, “The aerodynamics of insect flight.,” *J. Exp. Biol.*, vol. 206, no. Pt 23, pp. 4191–4208, 2003.

[20] M. H. Dickinson and K. Gotz, “Unsteady aerodynamic performance of model wings at low reynolds numbers,” *J. exp. Biol.*, vol. 174, pp. 45–64, 1993.

[21] Z. J. Wang, “Dissecting Insect Flight,” *Annu. Rev. Fluid Mech.*, vol. 37, no. 1, pp. 183–210, 2005.

[22] T. L. Hedrick, B. Cheng, and X. Deng, “Wingbeat Time and the Scaling of Passive Rotational Damping in Flapping Flight,” *Science.*, vol. 324, no. 5924, pp. 252–255, 2009.

[23] S. P. Sane, “Eppur si vola (and yet it flies),” *J. Exp. Biol.*, vol. 220, no. 4, pp. 514–516, 2017.

[24] T. Weis-Fogh, “Quick Estimates of Flight Fitness in Hovering Animals, Including Novel Mechanisms for Lift Production,” *J. Exp. Biol.*, vol. 59, no. 1, pp. 169–230, 1973.

[25] C. P. Ellington, C. van den Berg, A. P. Willmott, and A. L. R. Thomas, “Leading-edge vortices in insect flight,” *Nature*, vol. 384, no. 6610, pp. 626–630, 1996.

[26] M. J. Lighthill, “On the Weis-Fogh mechanism of lift generation,” *J. Fluid Mech.*, vol. 60, no. 1, p. 1, 1973.

[27] T. Weis-Fogh, “Unusual mechanisms for the generation of lift in flying animals,” *Sci. Am.*, vol. 233, pp. 81–87, 1975.

[28] C. P. Ellington, “Wing mechanics and take-off preparation of Thrips (Thysanoptera),” *J. Exp. Biol.*, vol. 85, no. January 1980, pp. 129–136, 1980.

[29] L. A. Miller and C. S. Peskin, “Flexible clap and fling in tiny insect flight,” *J. Exp. Biol.*, vol. 212, pp. 3076–3090, 2009.

[30] F. O. Lehmann and M. H. Dickinson, “The control of wing kinematics and flight forces in fruit flies (Drosophila spp.),” *J. Exp. Biol.*, vol. 201, pp. 385–401, 1998.

[31] Z. J. Wang, “Two Dimensional Mechanism for Insect Hovering,” *Phys. Rev. Lett.*, vol. 85, p. 2216, 2000.

[32] L. A. Miller and C. S. Peskin, “When vortices stick: an aerodynamic transition in tiny insect flight,” *J. Exp. Biol.*, vol. 207, pp. 3073–3088, 2004.

[33] T. Maxworthy, “Experiments on the Weis-Fogh mechanism of lift generation by insects in hovering flight. Part I. Dynamics of the fling.,” *J. Fluid Mech.*, vol. 93, pp. 47–63, 1979.

[34] R. B. Srygley and A. L. R. Thomas, “Unconventional lift-generating mechanisms in free-flying butterflies,” *Nature*, vol. 420, pp. 660–664, 2002.

[35] W. Shyy, “Flapping Wings and Aerodynamic Lift: The Role of Leading-Edge Vortices,”

AIAA, vol. 45(12), pp. 2817–2819, 2007.

[36] H. Liu and H. Aono, "Size effects on insect hovering aerodynamics: an integrated computational study," *Bioinspir. Biomim.*, vol. 4, pp. 1748–3182, 2009.

[37] J. G. Morse and M. S. Hoddle, "Invasion Biology of Thrips," *Annu. Rev. Entomol.*, vol. 51, no. 1, pp. 67–89, 2006.

[38] C. A. Schneider, W. S. Rasband, and K. W. Eliceiri, "NIH Image to ImageJ: 25 years of image analysis," *Nat. Methods*, vol. 9, no. 7, pp. 671–675, 2012.

[39] M. Masumoto, Y. F. Ng, and S. Okajima, "A new genus of Thripinae (Thysanoptera, Thripidae) collected from Pandanus in Japan, Malaysia and Australia, with three new species," *Zootaxa*, vol. 3709, no. 6, pp. 543–554, 2013.

[40] L. A. Miller and C. S. Peskin, "A computational fluid dynamics study of `clap and fling' in the smallest insects," *J. Exp. Biol.*, vol. 208, pp. 195–212, 2005.

[41] B. L. Smith and D. R. Neal, "Particle Image Velocimetry," Chapter 48, *Handbook of Fluid Dynamics*, Second Edition. 2016.

[42] A. Y. L. Cheer and M. A. R. Koehl, "Paddles and Rakes: Fluid Flow Through Bristled Appendages of Small Organisms," *J. Theor. Biol.*, vol. 129, pp. 17–39, 1987.

[43] J. Zhou, R. J. Adrian, S.Balachandar, and T. M. Kendall, "Mechanisms for generating coherent packets of hairpin vortices in channel flow," *J. Fluid Mech.*, vol. 387, pp. 353–396, 1999.

[44] A. Santhanakrishnan, I. Okafor, G. Kumar, and A. P. Yoganathan, “Atrial systole enhances intraventricular filling flow propagation during increasing heart rate,” *J. Biomech.*, vol. 49, no. 4, pp. 618–623, 2016.

[45] K. C. Stewart, C. L. Niebel, S. Jung, and P. P. Vlachos, “The decay of confined vortex rings,” *Exp. Fluids*, vol. 53, no. 1, pp. 163–171, 2012.

[46] J. C. Wu, “Theory for aerodynamic force and moment in viscous flows.,” *AIAA J.*, vol. 19, pp. 432–441, 1981.

[47] F. O. Lehmann, S. P. Sane, and M. Dickinson, “The aerodynamic effects of wing-wing interaction in flapping insect wings.,” *J. Exp. Biol.*, vol. 208, no. Pt 16, pp. 3075–92, 2005.

[48] A. Cavalleri and L. A. Mound, “Toward the identification of Frankliniella species in Brazil (Thysanoptera, Thripidae),” *Zootaxa*, vol. 30, no. 3270, pp. 1–30, 2012.

[49] M. Mirab-balou, X. Tong, and X. Chen, “A new record and description of a new species of the genus Thrips, with an updated key to species from Iran,” *J. Insect Sci.*, vol. 12, no. 90, pp. 1–15, 2012.

[50] É. F. B. Lima and L. A. Mound, “Species-richness in Neotropical Sericothripinae (Thysanoptera: Thripidae),” vol. 4162, no. 1, pp. 1–45, 2016.

[51] L. H. Dang, L. A. Mound, and G. X. Qiao, *Conspectus of the Phlaeothripinae genera from China and Southeast Asia (Thysanoptera, Phlaeothripidae)*, vol. 3807, no. 1. 2014.

[52] P. W. Gorham, “Ballooning Spiders: The Case for Electrostatic Flight,” *ArXiv*, p. 1309.4731v1 [physics.bio-ph], 2013.

[53] H. Ai, “Sensors and sensory processing for airborne vibrations in silk moths and honeybees.,” *Sensors (Basel).*, vol. 13, no. 7, pp. 9344–9363, 2013.

[54] H. Ai, A. Yoshida, and F. Yokohari, “Vibration receptive sensilla on the wing margins of the silkworm moth Bombyx mori,” *J. Insect Physiol.*, vol. 56, no. 3, pp. 236–246, 2010.

[55] G. Liu, H. Dong, and C. Li, “Vortex dynamics and new lift enhancement mechanism of wing–body interaction in insect forward flight,” *J. Fluid Mech.*, vol. 795, no. 2016, pp. 634–651, 2016.

APPENDICES

Matlab code for filtering force data

Following functions were used to filter the raw force data.

Step 1: Import the raw force data using following function.

```
function ImportedData = importData(filename,sampleLength)

ImportedData = zeros(sampleLength,30);

% %filename = 'V:\Insect Flight\Matlab\ClapDragForceRe5(old L Bracket).xlsx';

 for n=2:31

    ImportedData(:,n-1) = xlsread(filename,n,'A2:A104001');

    disp(n)

 end

% ImportedData = filename;
```

Step 2 : Filter the raw data using zero-phase delay, third order, low-pass digital Butterworth filter with cutoff frequency varying from 12-35 Hz.

```
function FilteredData = filterdata(ImportedData)

 [b,a] = butter(3,0.000465);

[sos,g] = tf2sos(b,a);

FilteredData = filtfilt(sos,g,ImportedData);

end
```

VITA

VISHWA TEJA KASOJU

Candidate for the Degree of

Master of Science

Thesis: CLAP AND FLING INTERACTION OF BRISTLED WINGS: EFFECTS OF VARYING REYNOLDS NUMBER AND BRISTLE SPACING ON FORCE GENERATION AND FLOW STRUCTURES

Major Field: Mechanical and Aerospace engineering

Biographical:

Education:

Completed the requirements for the Master of Science in Mechanical and Aerospace Engineering at Oklahoma State University, Stillwater, Oklahoma in May 2017.

Completed the requirements for the Bachelor of Engineering in Mechanical Engineering at Osmania University, Hyderabad, India in 2013.

Experience:

Professional Memberships: Member of American Physical Society.